NeuroImage 309 (2025) 121088

Contents lists available at ScienceDirect

NeuroImage

journal homepage: www.elsevier.com/locate/ynimg

Spontaneous mesoscale calcium dynamics reflect the development of the modular functional architecture of the mouse cerebral cortex

Davide Warm, Davide Bassetti [1], Levente Gellèrt [2], Jenq-Wei Yang, Heiko J. Luhmann, Anne Sinning [*]

Institute of Physiology, University Medical Center of the Johannes Gutenberg University, Duesbergweg 6, 55128 Mainz, Germany

ARTICLE INFO

Keywords:
Development
Cerebral cortex
Spontaneous activity
GCaMP6s
Wide-field microscopy
Calcium imaging
Network modularity

ABSTRACT

The mature cerebral cortex operates through the segregation and integration of specialized functions to generate complex cognitive states. In the mouse, the anatomical and functional correlates of this organization arise during the perinatal period and are critically shaped by neural activity. Understanding how early activity patterns distribute, interact, and generate large-scale cortical dynamics is essential to elucidate the proper development of the cortex. Here, we investigate spontaneous mesoscale cortical dynamics during the first two postnatal weeks by performing wide-field calcium imaging in GCaMP6s transgenic mice. Our results demonstrate a marked change in the spatiotemporal features of spontaneous cortical activity across fine stages of postnatal development. Already after birth, the cortical hemisphere presents a primordial macroscopic organization, which undergoes a steady refinement based on the parcellation of the cortex. As calcium activity transitions from large, widespread events to swift waves between the first and second postnatal week, significant topographic differences emerge across different cortical regions. Functional connectivity profiles of the cortex gradually segregate into main subnetworks and give rise to a highly modular network topology at the end of the second postnatal week. Overall, spontaneous mesoscale activity reflects the maturation of cortical networks, and reveals critical breakpoints in the development of the functional architecture of the cortex.

1. Introduction

The cerebral cortex operates through the functional segregation and hierarchical integration of neuronal modules, thus generating local and coherent patterns of activation (Sporns, 2013; Yuste et al., 2024). This modular organization is constitutive of the brain at different scales (Casanova and Casanova, 2019; Meunier et al., 2010), and reflects the need to process different sensory inputs and coordinate them with motor control to orchestrate behavior (De Schotten and Forkel, 2022; Petersen, 2019). The functionalization of different cortical regions, i.e. the arealization of the cortex (Van Essen and Glasser, 2018), occurs during early development, through the interaction of intrinsic genetic programs and neuronal activity-dependent mechanisms (Cadwell et al., 2019). While the former determine at embryonic stages a rough initial parcellation of the primordial cortex, known as protomap (Appan et al., 2023), the latter unfold during the perinatal phase in rodents (Martini et al., 2021) and regulate different cellular processes such as migration, differentiation, apoptosis, and synaptic wiring. Together they shape neuronal circuits in developing cortical areas (Cossart and Garel, 2022; Luhmann et al., 2016).

In the neonatal rodent brain, neuronal activity presents a stereotypical developmental sequence and a distinct spatial organization within individual cortical regions (Nakazawa and Iwasato, 2021; Wu et al., 2024). During the first postnatal days, cortical activity is strongly correlated in local networks and characterized by discontinuous high-frequency discharges, namely spindle bursts and gamma

* Corresponding author.
E-mail address: asinning@uni-mainz.de (A. Sinning).
[1] Current Address: Faculty of Mathematics, RPTU Kaiserslautern-Landau, Gottlieb-Daimler-Str. 48, 67,663 Kaiserslautern, Germany
[2] Current Address: MTA-SZTE "Momentum" Oscillatory Neuronal Networks Research Group, Department of Physiology, University of Szeged, Szeged, 6720, Hungary

https://doi.org/10.1016/j.neuroimage.2025.121088
Received 8 November 2024; Received in revised form 31 January 2025; Accepted 12 February 2025
Available online 13 February 2025

oscillations, observed both in primary sensory cortices (Hanganu et al., 2006; Mizuno et al., 2018; Yang et al., 2009) and in the primary motor cortex (An et al., 2014; McVea et al., 2012). At this early phase, local differences in event frequency and spectral power have been described (Blanquie et al., 2017), before neuronal activity becomes generally sparser and more decorrelated during the second postnatal week (Mòdol et al., 2024; Rochefort et al., 2009). As a result, response selectivity in sensory cortices (Van Der Bourg et al., 2017) and complex movement representations in the motor cortex (Glanz et al., 2021) are engendered. In mature circuits, network desynchronization supports efficient information processing (Olshausen and Field, 2004).

Remarkably, early neural dynamics occur spontaneously in the absence of overt behavior, i.e. when the animal is at rest or asleep (Blumberg et al., 2022; Colonnese and Khazipov, 2012), and are only gradually shaped by the maturation of sensory organs and their subcortical transduction pathways (Leighton and Lohmann, 2016). While myoclonic twitches, retinal waves and cochlear inputs partly contribute to local network discharges, (Ackman et al., 2012; Babola et al., 2018; Khazipov et al., 2004), the mechanisms which regulate the emergence of spontaneous activity patterns and their integration in large-scale waves remain largely unknown. With further development, the onset of active whisking (Van Der Bourg et al., 2017), responses to wake-related movements (Dooley and Blumberg, 2018), opening of ear canals (Meng et al., 2021) and eye lids (Shen and Colonnese, 2016) expand the repertoire of activity patterns in the cerebral cortex. At the same time, this rising cortical activation becomes increasingly regulated by the maturation of the GABAergic system (Warm et al., 2022b).

Hence, spontaneous activity in newborn mice appears as a highly dynamic process in space and time, which feeds back on the cytoarchitectonic structure of cortical areas, refining their topography, layer-specific cell distribution, and synaptic connectivity (Kirkby et al., 2013). Alterations in the physiological deployment of cortical activity (Guillamón-Vivancos et al., 2022; Henschke et al., 2017; Moreno-Juan et al., 2017; Siegel et al., 2012) have dramatic effects on the structure and function of cortical regions (López-Bendito et al., 2022; Nwabudike and Che, 2024) and the ensuing abnormalities in local and long-range connectivity can thus affect the cortex network organization, potentially causing cognitive impairments, i.e. autism spectrum disorders (Hutsler and Casanova, 2016). Therefore, understanding how local spontaneous neuronal activity develops and organizes throughout the cortex, and how the initial patterning correlates with the maturation of functional regions and network architecture, is fundamental to delineate proper neural development and to detect deviations with a prognostic value (Luhmann et al., 2022). While the current knowledge in the field mostly derives from electrophysiological and imaging studies with specific regional foci or restricted temporal windows, we here aim to provide a comprehensive overview of spontaneous activity in the early postnatal cortex and describe the fine-scale developmental trajectory of complex cortical dynamics of yet elusive origin.

For this purpose, we performed pan-hemispheric wide-field calcium imaging in lightly anaesthetized Snap25–2A-GCaMP6s-D mice to monitor mesoscale cortical dynamics during the first two postnatal weeks. Through different analytical approaches, we revealed several organizational principles of the mouse postnatal cortex, but also assessed the informative value of different methods for critical transitions in cortical network activity during early development. In detail, we investigated the developing functional parcellation of the cortex and quantified the level and complexity of cortical activity across time and space. Exploiting the anatomical segmentation of the mature cortex, we described the distribution and propagation of calcium waves within and across cortical areas and reconstructed the developing network architecture of the cortex.

2. Methods

2.1. Experimental model and techniques

2.1.1. Animals

All animal experiments conducted in this work were in accordance with national and European laws for the use of animals in research (2010/63/EU) and were approved by the local ethical committee (Landesuntersuchungsamt Rheinland-Pfalz, # 23 177–07/G 20–1–006). B6.Cg-*Snap25*$^{tm3.1Hze}$/J (common name: Snap25–2A-GCaMP6s-D) mice were obtained from The Jackson Lab (JAX stock # 025111, Bar Harbor, Maine, USA). The Snap25–2A-GCaMP6s-D mouse line is a knock-in model of the viral 2A oligopeptide and GCaMP6s (Chen et al., 2013) sequences, both inserted downstream of the synaptosomal-associated protein 25 (*Snap25*) coding region. This strategy provides a pan-neuronal and widespread expression of the GCaMP6s fluorescent sensor in the brain (Madisen et al., 2015). The B6.Cg-*Snap25*$^{tm3.1Hze}$/J mouse colony was maintained in the local animal facility by crossing heterozygous animals with wild-type C57BL/6J (JAX stock # 000664) mice. Pregnant mothers were checked every 24 h for birth of newborns. Genotyping of the offspring was done with standard polymerase chain reaction (PCR) assay (JAX protocol # 29906). Experiments were carried out acutely on Snap25–2A-GCaMP6s-D mouse pups of age comprised between postnatal day (P) 0 and 15. In total, 46 mouse pups of male and female sex were randomly assigned to age groups of 2- to 3- day spans. In total, mice from 22 different litters were used and each age group comprised animals from at least 3 independent litters (P0–2, $n = 5$ mice from 3 litters; P3–4, $n = 5$ mice from 4 litters; P5–6, $n = 9$ mice from 6 litters; P7–8, $n = 8$ mice from 6 litters; P9–10, $n = 6$ mice from 5 litters; P11–12, $n = 6$ mice from 5 litters; P13–15, $n = 7$ mice from 6 litters).

2.1.2. Animal surgery

Surgery was performed to enable optical imaging of the brain in head-fixed mice in vivo after the surgical exposure of the skull. Before the surgical procedure, animals were lightly anesthetized via intraperitoneal injection of urethane (1 mg/g, Cat. # U2500, Sigma-Aldrich, Merck, Darmstadt, Germany) and kept on a heating pad at 37 °C (TMP-5b, Supertech, Pecs, Hungary) to maintain body temperature. To minimize animal distress, the analgesic drug carprofen (5 mg/kg, Rimadyl®, Zoetis LLC, Parsippany, New Jersey, USA) was administered subcutaneously and the local anesthetic lidocaine 2.5 % - prilocaine 2.5 % (Emla, Aspen Pharma, Dublin, Ireland) gel was topically applied on the scalp. In addition, during the surgical procedure, a deeper anesthetic state was induced through inhalation of isoflurane 0.5–1.5 % (Piramal Critical Care, Hallbergmoos, Germany). After the excision of the scalp and of the underlying periosteum, the skull was cleaned and the bregma point was highlighted with a fine marker dot. A custom-made aluminum head-post was mounted onto the head with cyanoacrylate glue (Permabond LLC, Pottstown, Pennsylvania, USA) and animals were held firmly through a custom-made frame. To stabilize the preparation, low-melting agarose 1.5 % (Cat. #, 850080, Biozym Scientific GmbH, Hessisch Oldendorf, Germany) was applied onto the soft skull within the head-post boundaries, and a glass coverslip was placed on top and sealed with petroleum jelly (Engelhard Arzneimittel GmbH & Co., Niederdorfelden, Germany). Because even low dose isoflurane reduces neuronal discharge patterns, its inhalation was discontinued after transferring the mice to the recording chamber (at least 45 minutes before recording). The subsequent imaging was then performed under low dose of urethane and the depth of anesthesia was continuously checked by monitoring breathing rate and paw pinch reflexes throughout the experiment.

2.1.3. Wide-field calcium imaging

Wide-field calcium imaging of the right cortical hemisphere was performed through an upright microscope (BX51WI, Olympus, Tokyo, Japan) with a 1.25 × objective (PLAPON1.25X, Olympus) connected to a CCD camera (XM10, Olympus) and a mercury lamp light source (X-Cite 120, Excelitas Technologies Corp., Waltham, Massachusetts, USA). A green filter set was used (Excitation 480/30 nm bandpass filter, Dichroic Mirror AT 505, Emission 515 nm longpass filter). To center the curved surface of the cortical hemisphere within the field of view, the mouse head was tilted of ~30° by rotating the anchoring bar through a ball joint. Time-lapse videos were acquired with the cellSens software (Olympus) at a sampling frequency of 5 Hz and with a pixel binning of 2 × 2 (Fig. 1**A**). For each animal, spontaneous cortical activity was recorded in a 10-minute session (Videos S1–7), whereas sensory-evoked activity was subsequently captured over 20 trials, each lasting 20 s (Video S8). In a subset of experiments, a second 10-minute video session of spontaneous activity was recorded at least 2 h apart from the previous. Data from the latter are only shown in **Fig. S1**.

2.1.4. Sensory stimulation

Tactile stimulations of single whiskers were provided with a stainless-steel rod (1 mm diameter) connected to a miniature solenoid actuator. The rod was carefully positioned against single whiskers in perpendicular manner and close to the mouse snout. In particular, longer vibrissae belonging to columns B–C and rows 1–2 of the mystacial pad array were selected. Individual rod touches induced a displacement of the whisker of ~1 mm in the rostro-caudal direction. In a limited subset of experiments, auditory and visual stimulations were performed for validation purposes with a short (10 ms) sound (pure-tone of 10 kHz) or light pulse, respectively induced through a full-range loudspeaker and a standard LED. Repeated evoked responses were synchronized with a pulse generator (Master-8, A.M.P.I., Jerusalem, Israel) connected to the stimulation devices and to a real-time controller (U-RTC, Olympus) (**Fig. S1A**, left).

2.2. Data analysis and statistics

2.2.1. Image preprocessing

2.2.1.1. Spatial registration and image correction. In order to compare the neural activity across cortical hemispheres of increasing size during development, time-lapse videos were spatially registered to a common atlas-based reference map (see section below, *Cortical region characterization*). This procedure was implemented using a custom written routine as follows in detail. First, a graphical projection of the sensory evoked responses in the barrel field was drawn using the open-source software Fiji (**Fig. S1A**, right). For each whisker, a single $\Delta F/F_0$ video was computed by averaging the repeated stimulation trials and by considering the average time-projection of the video as the baseline fluorescence F_0. Single barrels were then outlined by manually thresholding the standard deviation time-projection of the peristimulus frames (i.e. within 3 s from the stimulation trigger) and overlaying this onto the F_0 image. The resultant picture was imported in MATLAB 9.11 (The MathWorks Inc., Natick, Massachusetts, United States) to find the registration coordinates through a graphical user interface. These included bregma, lambda and the barrels anatomical landmarks. By matching the latter with the corresponding points of the reference map, the image was aligned (*imrotate*), scaled (*imscale*) and geometrically transformed. In particular a piece-wise linear transformation object was obtained through the *fitgeotrans* function and applied through the *imwarp* function. After visually checking the result of the spatial registration (see Fig. 1**B**, middle), the coordinates were saved and used to register the time-lapse video. Henceforth, all analysis were performed in MATLAB.

To perform subsequent computational-intensive analysis, time-lapse frames of 688 × 516 pixels were down-sampled by an 8 × 8 binning to a size of 86 × 65 pixels. The videos were then corrected to account for common sources of artifacts in fluorescence imaging (**Fig. S1B**). First, videos were motion-corrected using the *NoRMCorre* algorithm (Pnevmatikakis and Giovannucci, 2017). Subsequently, to compensate for intensity drift over time, fluorescence values across frames were divided by a normalized background trace. The latter was computed as the average fluorescence of the background area (i.e. pixels lying outside the hemisphere borders of the reference map) divided by its temporal minimum. Finally, to correct for uneven illumination, due to spherical aberration of the epi-fluorescence microscope objective and to the hemispheric curvature of the brain (x-y dimensions), fluorescence values within each frame were divided by a spatial mask, calculated as a normalized minimum time-projection of the video. While binning and spatial correction mitigated the effect of small vasculature, no further hemodynamic correction was applied to keep data preprocessing uniform across age groups since the neurovascular response in young animals appears to be absent or significantly reduced even until the end of the second postnatal week (Kozberg et al., 2016).

2.2.1.2. Signal unit conversion and intrinsic properties. Video fluorescence values were converted to $\Delta F/F_0$ units (Fig. 1**B**, right) using the open-source toolbox from Romano et al. (2017). In particular, after reshaping the video 3D matrix into a 2D array (m frames × *n* pixels), the pixelwise baseline fluorescence F_0 was estimated using a running-window average of the pixel fluorescence trace (F_{smooth} option), whereas the pixelwise baseline fluorescence noise σ was estimated by fitting a Gaussian model to the negative fluctuations of the pixel $\Delta F/F_0$ trace (*Gaussian model* option).

The signal intensity, frequency and entropy were computed for each $\Delta F/F_0$ pixel trace (Fig. 1**C**) and their average value across space sampled for each animal. Relative intensity was calculated as the maximum time-projection. The signal peak frequency was computed adapting a MATLAB code (Uhlén, 2004) for the calculation of power spectral density. Traces were padded with zeros until 4096 points and the peak frequency value was stored. A lowpass filter of 1 Hz was applied to discard noisy pixels from the analysis. Entropy was calculated with the homonymous MATLAB built-in function.

2.2.2. Cortex functional segmentation

2.2.2.1. Correlation analysis. To identify macroscale spatial organization principles, we segmented the cortex in a data-driven manner (Fig. 2**A**), following a similar approach to White et al. (2011). For each animal, a correlation matrix was computed by calculating the pairwise Pearson coefficient between the pixel $\Delta F/F_0$ traces. To obtain age group representations, correlation matrices of animals belonging to the same age group were averaged. Starting from individual or age group matrices, we performed hierarchical clustering via average Euclidean linkage based on the following distance metric:

$$D(x,y) = 1 - C(x,y)$$

where $C(x,y)$ is the correlation between pixels x and y. High-level clusters were then identified by cutting the hierarchical tree at a threshold value of 15.5. This parameter was selected upon visual

inspection of the dendrograms, and applied uniformly across animals and age groups. The univocal cluster identity for each pixel was then color-coded to display the cortical parcels. To additionally visualize the spatial extent of macroscopic domains, seed-based correlation maps were created by plotting the Pearson coefficient values computed in relation to specific pixel locations (i.e. one line of the average correlation matrix). Seed locations were chosen based on the centroids of main anatomical regions (see section below, *Cortical region characterization*).

2.2.2.2. Non-negative matrix factorization. To characterize mesoscopic cortical domains and exclude potential non-neuronal confounders from the functional segmentation (Quarta et al., 2022), we applied non-negative matrix factorization (NMF) (**Fig, S3A**), a technique, which has been widely used in calcium imaging data for blind source separation (Maruyama et al., 2014). By reshaping the three-dimensional video ($x \times y \times t$ pixels) into a 2D array V (m [$x \times y$] rows $\times$ n [t] columns), NMF can be employed to decompose the data into a component matrix W and a coefficient matrix H, whose product provides an approximation of the original video:

$$V(m \times n) \approx W(m \times k) \times H(k \times n)$$

where k is the pre-specified rank of the factorization. The latter is generally a low value such that $(m+n)\cdot k < (m \times n)$ and represents the number of latent components in the decomposition (in our case, the number of parcels).

Importantly, NMF imposes a non-negativity constraint on the input and output matrices, which can nicely capture the positive $\Delta F/F_0$ fluctuations of calcium transients. To meet this condition and exclude potential camera noise from the reconstruction, pixels, whose $\Delta F/F_0$ values were below a threshold, defined as 5 times the baseline noise σ above the baseline mean μ, were set to 0. Moreover, the $\Delta F/F_0$ frames were denoised by applying a median filter (*medfilt2*) and a gaussian smoothing (*imgaussfilter,* $\sigma = 3$). The ensuing *denoised* $\Delta F/F_0$ video was reshaped and iteratively processed with the built-in *nnmf* function to find the optimal value of k within the range between 1 and 51. The upper bound on the number of k was selected based on the maximal intrinsic dimensionality across datasets (i.e., the number of PCA components needed to explain 90 % of the variance, see **Fig. S3F**). Then, for each video, the appropriate value within the range of k was found, using the fraction of variance explained (*FVE*) by the reconstruction as a quality metric. The latter was calculated as:

$$FVE = 1 - \frac{\sum_{m=1}^{M}\sum_{n=1}^{N}(V - WH)^2}{\sum_{m=1}^{M}\sum_{n=1}^{N}V^2}$$

where the denominator expresses the sum of squares of the original matrix, and the numerator is the sum of squares of the residuals. As the NMF does not provide unique solutions, but rather converges to a local minimum depending on the initial conditions, three repetitions were run for each value of k. After averaging the resulting *FVE* values, the optimum k was selected as the first index in the range where the *FVE* was larger than 90 %. In the few cases, where this condition was not met, the value corresponding to the maximum *FVE* was used. Finally, out of the three repetitions, the decomposition with the highest *FVE* was retained for subsequent analysis.

To be able to compare experiments and considering that each factor can be scaled without changing the solution, matrix W and H were normalized, dividing each column W_k by its maximum value, and multiplying each row H_k by the same factor. This procedure effectively scales each spatial component such that its values belong to the closed interval [0,1], while the activations are allowed to take any positive real value. Cortical domains were then defined as the largest core region of each spatial component W_k, that resulted after applying the following threshold: 2 times the mean of W_k positive values. In case no core region was found, the threshold multiplier was iteratively lowered by a value of 0.5. Overlap of cortical domains was then calculated as the average set union between core region pairs and expressed in % units of hemispheric area. Representative functional maps were generated by summing all component projections, individually computed as the Euclidean norm of H_k. To quantify the localization of cortical domains, the spatial indices of the apical point (W_k maximum) were found and sorted into one of the four partitions of the hemisphere (**Fig. S3G**). The latter were outlined in roughly equally-sized sectors loosely corresponding to the main cortical lobes: frontal, parietal, temporal, and occipital.

2.2.3. Mesoscale calcium dynamics

2.2.3.1. Event morphological segmentation. To systematically characterize the optical features of complex spontaneous cortical dynamics, calcium events, i.e. non-contiguous calcium fluctuations in space and time, were isolated (Fig. 3**A**, top-left). To this end, a binary matrix of the *denoised* $\Delta F/F_0$ fluctuations (see section above, *Non-negative matrix factorization*) was obtained and processed through the following routine (built-in MATLAB function are indicated in parenthesis). First, small structures were removed from each frame, by applying a median filter (*medfilt2*) and removing residual connected components (*bwareafilt*) smaller than 20 pixels. Then, a morphological closing operation was performed by smoothing the edges with a gaussian filter (*imgaussfilter,* $\sigma = 1$) and eroding (*imerode*) them with a flat structural element (*strel*) object of size 1. The separation of three-dimensional structures was ensured by applying on the 3D binary matrix a further erosion step with a spherical *strel* object of size 1. Finally, connected components were numerically labeled (*regionprops3*).

With the described routine, the isolated calcium events consisted already of transients displaying 1 or few *temporal peaks* on their average $\Delta F/F_0$ trace. However, due to the high-intensity $\Delta F/F_0$ fluctuations in certain age groups and to the general slow kinetics of the GCaMP6s sensor, in a minority of cases (~12.5 %) event duration was considerably long, i.e. > 8 s, as determined by statistical analysis on the pooled dataset with *isoutlier* function and *quartiles* method. Therefore, to ensure that the root of these rare observations was a prolonged cortical activation and not the result of a long decaying tail, an additional thresholding procedure was applied taking into account the average $\Delta F/F_0$ trace of the event. In particular, frames, whose average $\Delta F/F_0$ value was below a threshold of 5 times the baseline noise σ above the baseline mean μ, were set to 0. μ and σ were computed as the average values across all pixels covered by the event. An analogous procedure was iterated on the few (~7.5 %) residual outlier (in this case, events > 20 s), by raising the baseline noise multiplier to 7. As a result, only *significant* $\Delta F/F_0$ fluctuations were retained for subsequent analysis.

Calcium events were extracted and morphologically characterized with the *regionprops3* function. Leveraging the output of the latter, the following spatiotemporal parameters (see also Fig. 3**A**, bottom-right) were calculated: *duration* (s), *amplitude* (maximum temporal peak), *area* (binary time-projection, in hemisphere %), *volume* (cumulative $\Delta F/F_0$), and average *circularity* (for frames with multiple components, the largest one was considered). In addition, *path distance* was computed as the sum of all pairwise Euclidean distances between two consecutive maxima points. To confirm results, values of area and path distance were also scaled according to the actual size of the hemispheres and expressed in units of mm and mm^2. Finally, in frames corresponding to the temporal peaks, *vertices* (i.e. local maxima points) were estimated with the open-source function *FastPeakFind* (MATLAB Central File Exchange) using a threshold value equal to the sum of the average baseline μ and

the average baseline noise σ of the pixels covered by the event.

2.2.3.2. Optical flow features. Optical flow analysis (Fig. 3**A**, top-right) was performed with the open-source toolbox provided by Afrashteh et al. (2017). Optical flow encompasses a class of algorithms developed in the sector of computer vision to estimate velocity vector fields from an image sequence, and enable the calculation of speed and motion direction of objects as well as the location of their sources and sinks. We chose the Horn-Schunck (HS) method due to its consolidated application and to the low number of parameters requiring to be tuned. In particular, the regularization constant α was fitted with a range of 10 values, using the number of identified sources and sinks in the lowest signal-to-noise ratio (SNR) videos (i.e. P0–2 age group) as a quality metric (**Fig. S4E, F**). An α value of 0.105 was selected based on the elbow method, whereas the number of iterations was maintained to 2000.

We then extracted each event matrix and analyzed it separately. To comply with the input conditions of the algorithm, each matrix z-section of 86 × 65 pixels was padded with zeros to an equal size of 128 × 128. In addition, zeros-frames were added at the start and end of the matrix, to estimate optical flow properties for the whole duration of the event. In this way, the input consisted of a 3D $\Delta F/F_0$ matrix of size $z = t + 2$, where t is the frame number of the event, and the output was a vector field matrix (i.e. a complex number array) of z-1 sections, describing the instantaneous flow between consecutive frame pairs. For each output z-section a unique *velocity vector* expressing the overall flow was estimated by combining the direction (i.e. phase angle of the conjugate value) of the vectorial field sum and its maximum magnitude (i.e. modulus) as vector length. Event *speed* in pixel per frame (px/f) units was then calculated as the average magnitude of velocity vectors, whereas *direction change* as the average angle difference (°/f) of adjacent velocity vectors computed after wrapping their radian values in the range $[-\pi, \pi]$. For validation purposes, estimates of speed were also converted to mm/s taking into account the absolute hemispheric size and the frame sampling rate. Sources and sinks were detected with the provided algorithm (Afrashteh et al., 2017) and their unique locations per event were found as follows. The output *struct* element could consist of multiple source or sink contours nested within the same z-section or overlapping across consecutive ones. Therefore, redundant sources or sinks were merged by converting the outlined areas to a mask (*poly2mask*) and obtaining a 3D binary matrix of independent sources or sinks. Distinct source or sink locations per event were then identified from the time-projections of the latter with the *regionprops* function. *Source to sink distance* was computed as the grand average of the pairwise distance between consecutive sources and sinks belonging to a calcium event.

2.2.4. Cortical region characterization

2.2.4.1. Atlas-based map. To delineate main cortical regions based on anatomical annotations, we derived the atlas-based reference map (Fig. 4**A**, left) from the 3D browser-based visualization tool, Allen Brain Explorer® beta (originally described in Lau et al., 2008). The 3D model of the cortical surface, delineating the main functional regions, was oriented to match the experimental conditions and its graphical projection was imported in the open-source software Inkscape. Cortical regions were traced accordingly, whereas the outlines of whisker barrels were obtained by vectorizing the barrel map from Petersen (2019). Finally, the map was cropped to match the field of view limits of the largest cortical hemisphere (P15) and converted to a rasterized version of 688 × 516 pixels. The latter was imported into MATLAB and binned to a matrix of size 86 × 65 with discrete region identifiers.

2.2.4.2. Activity distribution. Activity levels within cortical regions were quantified through the analysis of basic features of the signal and event related markers (Fig. 4**A**, middle). The former were extracted with slightly downsized masks of the cortical regions (*imerode* function with a disk *strel* object of size 3) to ensure the localization of signal. Using these masks, we computed both *average $\Delta F/F_0$ region traces* and the average properties of *significant* $\Delta F/F_0$ fluctuations (see section above, *Event morphological segmentation*). Through the latter, we obtained a binary trace, distinguishing between active and silent periods. For each region, *active time* was determined as the total fraction (in %) of active frames during the recording, whereas *inter-active time* as the average duration of silent intervals. *Intensity* was calculated as the maximum average $\Delta F/F_0$ value. *Area fraction* (in hemisphere %) was computed as the average active part of the region, during active frames. *Event rate* was computed as the number of events per minute that engaged each specific region. *Source* or *sink rates* per region were calculated as the number of independent sources or sinks per minute in each region. To this end, the centroids of connected components within each event 3D binary matrix of either sources or sinks (see section above, *Optical flow features*) were pooled together across the recording time, and sorted in the different cortical regions. Vertices coordinates were processed analogously to compute the region *vertex rates*. Finally, average pixel parameters of frequency, entropy, correlation, and parcellation (i.e. nr of cortical parcels per pixel) were computed across each region surface.

2.2.4.3. Activity propagation. The propagation of events across cortical regions was determined based on the rise phase of the event average $\Delta F/F_0$ trace, comprised between the first and the peak time frames (Fig. 4**A**, right). Events with more than one temporal peak were divided in correspondence to the valley time point between two consecutive peaks and were then analyzed separately. The event origin was determined as the maximum $\Delta F/F_0$ point at the starting frame, whereas the x-y coordinates of vertices were used to identify target regions. Based on the former, events were first sorted into the different cortical areas, and then for all events arising in one region, the proportions of target regions were computed. The latter were averaged across experiments of the same age group and presented as pie charts. Finally, the flow direction was determined by computing the sum between the velocity vectors of the event rising phase frames and by assigning the resulting angular value to one of eight polar histogram bins. These were centered along four main anatomical axis (A-P, M-L, AM-PL and AL-PM) and had a width of 45° (see also Fig. 4**A**, right). Probability polar histograms were then estimated for each experiment and their averages computed for each age group.

2.2.5. Network architecture

2.2.5.1. Functional connectivity. To describe the network architecture of the cortex, we measured functional connectivity using two standard metrics, Pearson correlation and mutual information. Both measures allow to determine statistical dependencies between pairs of signals and to draw undirected network graphs. However, while the correlation coefficient captures only linear relationship, mutual information, an information theory measure based on the concept of entropy, also captures nonlinear dependencies within the data (Fig. 6**A**). These metrics were applied between pairs of *average $\Delta F/F_0$ region traces* (see section above, *Activity distribution*) to characterize the high-level network organization across cortical areas. Conversely, to reconstruct functional connectivity within cortical regions, mutual information was also computed at an order of magnitude lower, after sampling average $\Delta F/F_0$ traces using a subregional map (**Fig. S7F**). The latter was obtained by scattering 316 seeding points across the cortical hemisphere and by delineating subregional patches through the open-source function

regiongrowing (MATLAB Central File Exchange). Pearson coefficient was calculated with the built-in *corrcoef* function, whereas mutual information was calculated as:

$$MI(X,Y) = H(X) + H(Y) - H(X,Y)$$

where $H(X)$ and $H(Y)$ are the marginal entropies of trace X and Y, and $H(X,Y)$ is the joint entropy between traces X and Y. The latter is in turn computed as

$$H(X,Y) = -\sum_{x\in X}\sum_{y\in Y} p(x,y)\log_2 p(x,y)$$

where $p(x,y)$ correspond to the joint probability of states x and y.

To exclude spurious connections from the analysis, surrogate data testing was performed on the obtained connectivity matrices. In detail, pairwise correlation and mutual information matrices were resampled after breaking the temporal structure within the data, as obtained by shifting the traces with different random offsets of ± 300 frames (i.e. 1 minute recording). Null-hypothesis distributions were then sampled by iterating this procedure 1000 times for region network and, due to high computational cost, 100 times for subregion networks. Statistically significant connections were retained at p values of 0.05, i.e. when their connectivity values were higher than the surrogate ones in > 950 or 95 cases, respectively. Finally, individual connectivity matrices were obtained per each animal and averaged per age group representations.

2.2.5.2. Graph theory. Network graphs (see, Fig. 6**E** and **S7E**) were constructed from undirected connectivity matrices, obtained after the following thresholding procedures. As a rule of thumb, one standard deviation above the median value of a connectivity matrix was used to find candidate threshold parameters depending on the type of network (region or subregion) or sample (individual animal or age group average). To compare region network features over development, but at the same time avoid the generation of unconnected networks, a *global threshold* was chosen as the minimum threshold value computed across all animal connectivity matrices. To visualize representative connectivity profiles per each age group, the global threshold was applied on the age group connectivity matrices and the resulting networks with undirected edges were plotted in MATLAB using the built-in function *graph*. In addition, relevant connections within each age group were overlaid on the same graphs after applying the respective age group threshold parameter (i.e. *local threshold*). Finally, to compare connectivity properties within cortical regions, the individual threshold computed on each subregion matrix was applied.

Starting from the obtained weighted or binary networks, graph properties were estimated using the brain connectivity toolbox (Rubinov and Sporns, 2010). In detail, *connection degree* and *strength* were computed as the average node degree and strength of the entire network. *Clustering coefficient* and *characteristic path length* were computed as the average values of nodes belonging to either the entire network or each cortical region. *Modularity* indices were determined with the provided Louvain community detection algorithm on both region and subregion networks.

2.2.6. Statistics

All statistical tests were performed using GraphPad Prism 10.2 (GraphPad, La Jolla, California, United States). Normality of sample distributions was tested with Shapiro-Wilk test. Direct comparisons between two groups were performed with Student unpaired or paired *t*-test for normally distributed data and with Mann-Whitney test for not normally distributed data. Multiple groups were compared using either one-way ANOVA followed by Tukey's multiple comparisons post-hoc test, or Kruskal-Wallis test (or Friedman test for paired data) followed by Dunn's multiple comparisons post-hoc test, depending on whether the normality test was passed. Two-way ANOVA followed by Tukey's multiple comparisons was used to quantify the interaction between different factors. Significance was considered at p values < 0.05. Throughout the text, data are reported as mean ± standard deviations (SD). Plot descriptions are provided in figure legends.

3. Results

3.1. Wide-field calcium signals reveal developmental changes in neuronal population dynamics

During early postnatal development, cerebral cortex activity is shaped through the dynamic interaction of spontaneously generated firing patterns and incoming sensory inputs progressively relayed from the periphery (Siegel et al., 2012; Yang et al., 2009). To investigate how local activation patterns distribute and integrate throughout the developing murine cortex, we performed pan-hemispheric wide-field calcium imaging on Snap25–2A-GCaMP6s-D animals (Madisen et al., 2015) during the first two postnatal weeks (Fig. 1**A**). Head-fixed mouse pups under light urethane anesthesia were acutely imaged through the intact skull with an epi-fluorescence microscope at single postnatal days (P) between P0 and P15. In each experimental session, spontaneous cortical activity was recorded followed by repeated evoked potentials via mechanical stimulation of single whiskers (**Videos S1–8**). The different trials were then averaged to visualize the sensory response within the barrel field. Combining the latter with anatomical landmarks of the skull, time-lapse videos were registered to a uniform reference map, allowing the systematic comparison across cortical hemispheres of growing sizes (**Fig. S1C**). While single whisker response was already evident shortly after birth, the alignment with functional regions of the cortex was exemplified in relation to auditory and visual stimuli, after hearing onset and eye opening (**Fig. S1D**). Then, the fluorescence signal was preprocessed and converted in $\Delta F/F_0$ units (Fig. 1**B** and **Video S9**).

Throughout our study, we investigated functional changes of the developing cortex across 7 different age groups, ranging 2 or 3 postnatal days each (P0–2, $n = 5$; P3–4, $n = 5$; P5–6, $n = 9$; P7–8, $n = 8$; P9–10, $n = 6$; P11–12, $n = 6$; P13–15, $n = 7$). Within these boundaries, we first studied the hemispheric average properties of the signal in the time and frequency domain, as well as on the information theoretic level (Fig. 1**C–F**). This analysis highlighted that the fluorescence intensity peaked at the end of the first postnatal week (from 5.98 ± 2.27 at P0–2 to 27.8 ± 7.51 % $\Delta F/F_0$ at P7–8, $p = 0.0011$, Dunn's multiple comparisons test) and then reduced (10.5 ± 4.05 % $\Delta F/F_0$ at P13–15 vs P7–8, $p = 0.011$, Dunn's multiple comparisons test), whereas its dominant frequency raised in between the first and the second postnatal week (from 22.4 ± 9.32 at P0–7, $n = 23$, to 35.3 ± 10.8 mHz at P8–15, $n = 23$, $p < 0.0001$, Student unpaired *t*-test). The quantification of signal entropy instead showed how the average information contained within calcium traces gradually increased reaching a plateau at P9–10 (from 1.45 ± 0.26 at P0–2 to 3.48 ± 0.46 bits at P9–10, $p < 0.0001$, Tukey's multiple comparisons test). To rule out major oscillations in neural activity depending on fluctuating anesthetic state (Erchova et al., 2002), we performed in a subset of experiments a second recording of spontaneous activity at least two hours apart and compared the measurements. None of the parameters showed significant differences across imaging sessions for any of the age groups (**Fig. S1E–G**).

Thus, wide-field fluorescence imaging on Snap25–2A-GCaMP6s-D animals enables stable and low-invasive acute recording of pan-cortical calcium dynamics during early development, and the monitoring of their physiological changes in time and space.

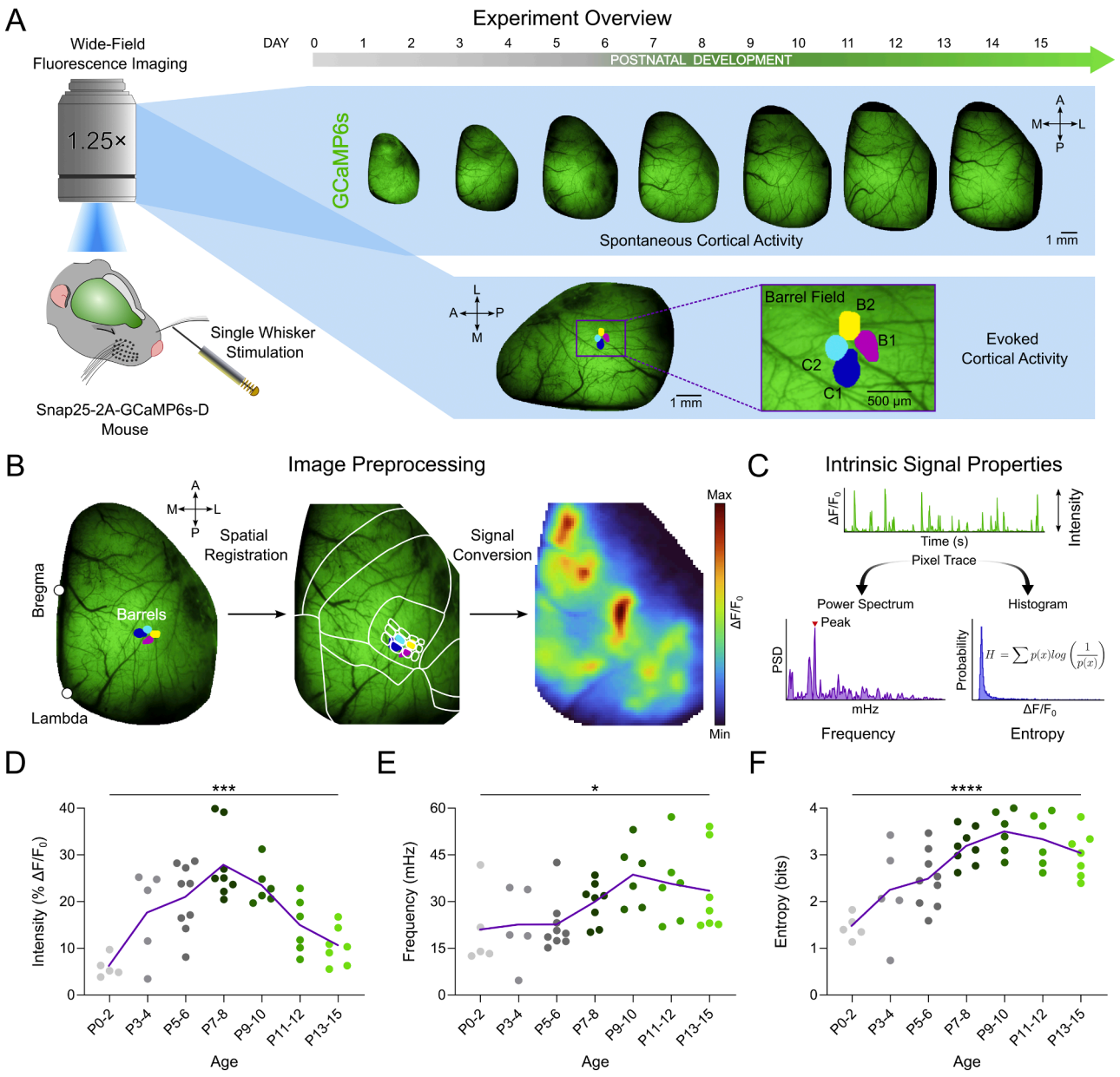

Fig. 1. Pan-hemispheric calcium dynamics in the developing mouse cortex. (**A**) Schematic overview of the experimental design. Animal experiments are conducted at single postnatal days (P) between P0 and P15 in Snap25–2A-GCaMP6s-D mice. Anesthetized mouse pups are head-fixed under an upright microscope and fluorescence imaging of the right cortical hemisphere is performed through the intact skull (top). Spontaneous activity is recorded in 10-minute time-lapse videos. Individual whisker barrels are outlined from the average response of 20 trials, in which evoked activity is induced through single whisker stimulations in the contralateral mystacial pad (bottom). A representative graphical projection of the sensory response is shown for a P7 mouse. (**B**) Image preprocessing steps. Individual videos are aligned to a common reference map and, after motion and background correction, converted into $\Delta F/F_0$ units. (**C**) Graphical scheme of intrinsic signal properties. For each pixel belonging to the cortical surface, a calcium trace is extracted and the following parameters are sampled: intensity (maximum value), frequency (peak of the power spectrum), and signal entropy. Signal intensity (**D**), frequency (**E**), and entropy (**F**) are averaged across the whole hemisphere and compared over different postnatal stages. Dot plots represent individual experiments, whereas lines (purple) indicate age group means. $^{*}p < 0.05$, $^{***}p < 0.001$, $^{****}p < 0.0001$, one-way ANOVA or Kruskal-Wallis test.

3.2. The functional parcellation of the cortex refines steadily over postnatal mouse development

In the cerebral cortex at rest, structural principles can be gathered from the linear relationship of spontaneous activity oscillations down to the infraslow frequency range (Chan et al., 2015). Here, we aimed to characterize the development of the functional cortical organization, by investigating the spatiotemporal interactions of the calcium signals across the hemisphere.

To identify the latent macroscopic structure of the data in an unsupervised manner, we first computed the Pearson coefficient ρ among pairs of pixel calcium traces and obtained correlation and distance matrices of the hemisphere for each animal and for each age group (Fig. 2**A**). Next, we hierarchically linked inter-dependent pixels and determined spatial domains by splitting the dendrograms at a constant threshold level. The analysis showed that, in line with a progressive signal decorrelation at hemispheric level (Fig. 2**B**, from a Pearson ρ of 0.40 ± 0.06 at P0–2 to 0.22 ± 0.04 at P13–15, $p = 0.0012$, Dunn's multiple comparisons test), the cluster number raised over time (Fig. 2**C**, from 4.4 ± 1.67 at P0–2 to 11 ± 3.22 at P13–15, $p = 0.0014$, Tukey's

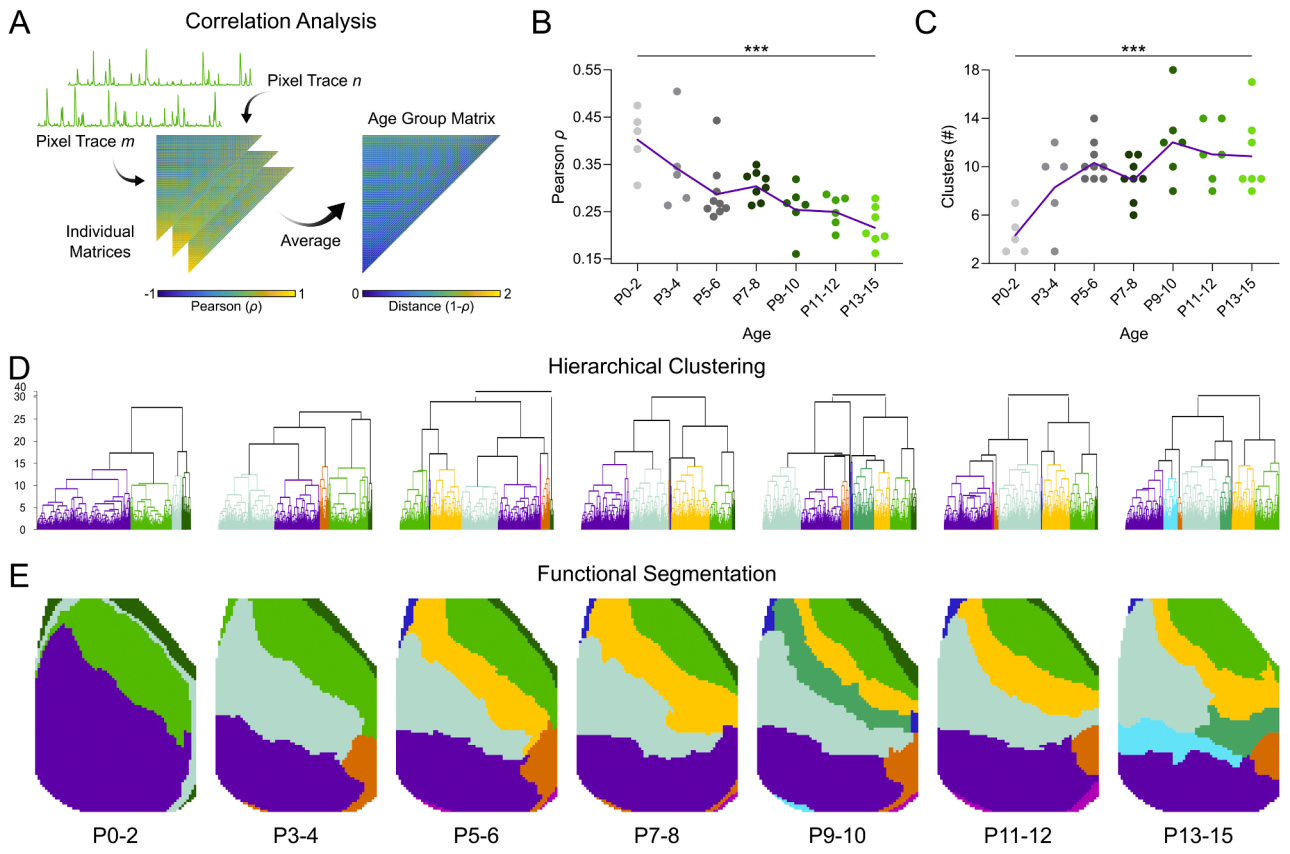

Fig. 2. Functional segmentation of macroscopic cortical parcels. (A) Graphical representation of the correlation analysis. For each recording, Pearson correlation matrices of single-pixel calcium traces are computed and averaged for age group representations. Spatial domains are identified for both individual and age group matrices through hierarchical clustering based on the Euclidean distance metric. The signal correlation is calculated as the average Pearson coefficient across the whole hemisphere (**B**), and is inversely related to the number of cortical domains (**C**) across development. Dot plots represent individual experiments, whereas lines (purple) indicate the age group mean. ***$p < 0.001$, one-way ANOVA or Kruskal-Wallis test. (**D**) Dendrograms of the age group hierarchical trees. A uniform threshold is applied to identify high-level clusters of inter-dependent pixels (color-coded). **(E)** Macroscopic spatial domains within the cortical hemisphere are colored based on the respective cluster identity.

multiple comparisons test). To illustrate the mean spatial organization of the cortex at different developmental stages, we color-coded the branches of the age group dendrograms and pinpointed their respective positions within the hemisphere accordingly (Fig. 2**D, E**). In addition, single animal reconstructions are shown in **Fig. S2A**. Together, these functional representations of the cortex denoted that although the number of clusters increased over development, a consistent layout orientation was already present from the first postnatal days. Starting from P3–4, the resulting outline highlighted a large posterior domain (purple), a medio-central area (turquoise), and multiple clusters in the frontal section (predominantly light-green and yellow) arranged along the antero-lateral axis of the hemisphere. This configuration consolidated in a more stable pattern from P5–6 onwards, with only minor variations in the extension and number of clusters within the lateral section (orange and sea-green). Interestingly, a closer examination of the bifurcations of the dendrograms revealed a tighter relation between the posterior (purple) and medio-central (turquoise) domains, as compared to the antero-lateral clusters, pointing out a higher-order pattern already evident at P0–2.

The employed clustering approach allowed the unbiased delineation of hemispheric functional areas and the comparison of cortical parcellation degree across different age groups. However, the hemispheric signal correlation can be impacted by age-dependent changes in global physiological parameters such as vasculature fluctuations or breathing rate, whereas the presence of small (blue and magenta) and thin-striped (dark green) clusters in our segmentation scheme, likely reflected spurious correlations due to the hemispheric curvature of the brain and/or minor alignment differences.

To corroborate the spatial orientation and the observed increase in the number of clusters, we additionally computed seed-based correlation maps (**Fig. S2B**) and performed blind source separation through non-negative matrix factorization (NMF) (**Fig. S3A**). Average correlation maps were created in relation to seeds (i.e. pixels) located at the centroids of main atlas-based areas. As expected, seed-based correlation maps reflected the orientation of the segmented clusters, but also highlighted a progressive refinement in the extension of functional domains. The latter closely matched the boundaries of the overlaid anatomical regions with the only stable exception of primary somatosensory and motor cortices, which displayed a tight relationship orthogonal to their demarcation line. On the other hand, NMF enabled to separate cortical activity sources from potential non-neuronal signal fluctuations (Quarta et al., 2022) and extract their mesoscopic outlines and temporal activation patterns. Its analysis confirmed a steady increase in the number of components across the first two postnatal weeks (**Fig. S3B**), whereas their areas were larger during the first postnatal week and progressively declined afterwards (**Fig. S3C**). In line with these divergent trends, the overlapping hemispheric portion between multiple functional domains (**Fig. S3D**) peaked at P7–8 and then decreased. These effects were exemplified by overlaying the identified cortical domain outlines of representative experiments onto hemispheric silhouettes and weighting their intensity values according to the activation level (**Fig. S3E**). While the outline of cortical domains was variable, in line with seed-based maps, a finer parcellation, but also a higher activation of the cortex was apparent over time. In addition, the hemispheric distribution of components changed with postnatal age from a mostly central sector, roughly corresponding to the parietal

region, to the caudal part of the cortex (**Fig. S3G–H**).

Overall, our results indicate how a macroscopic functional organization of the cortex is evident already after birth, and how a finer parcellation emerges while preserving the hierarchical structure of cortical domains. At the same time, coherent activation patterns engage cortical patches of decreasing sizes and overlap, suggesting a finer specialization of processing units and an increase in complexity of spontaneous activity.

3.3. *Mesoscale calcium dynamics present a marked developmental regulation of spatiotemporal properties*

The refinement in functional parcellation of the cortex underlies the

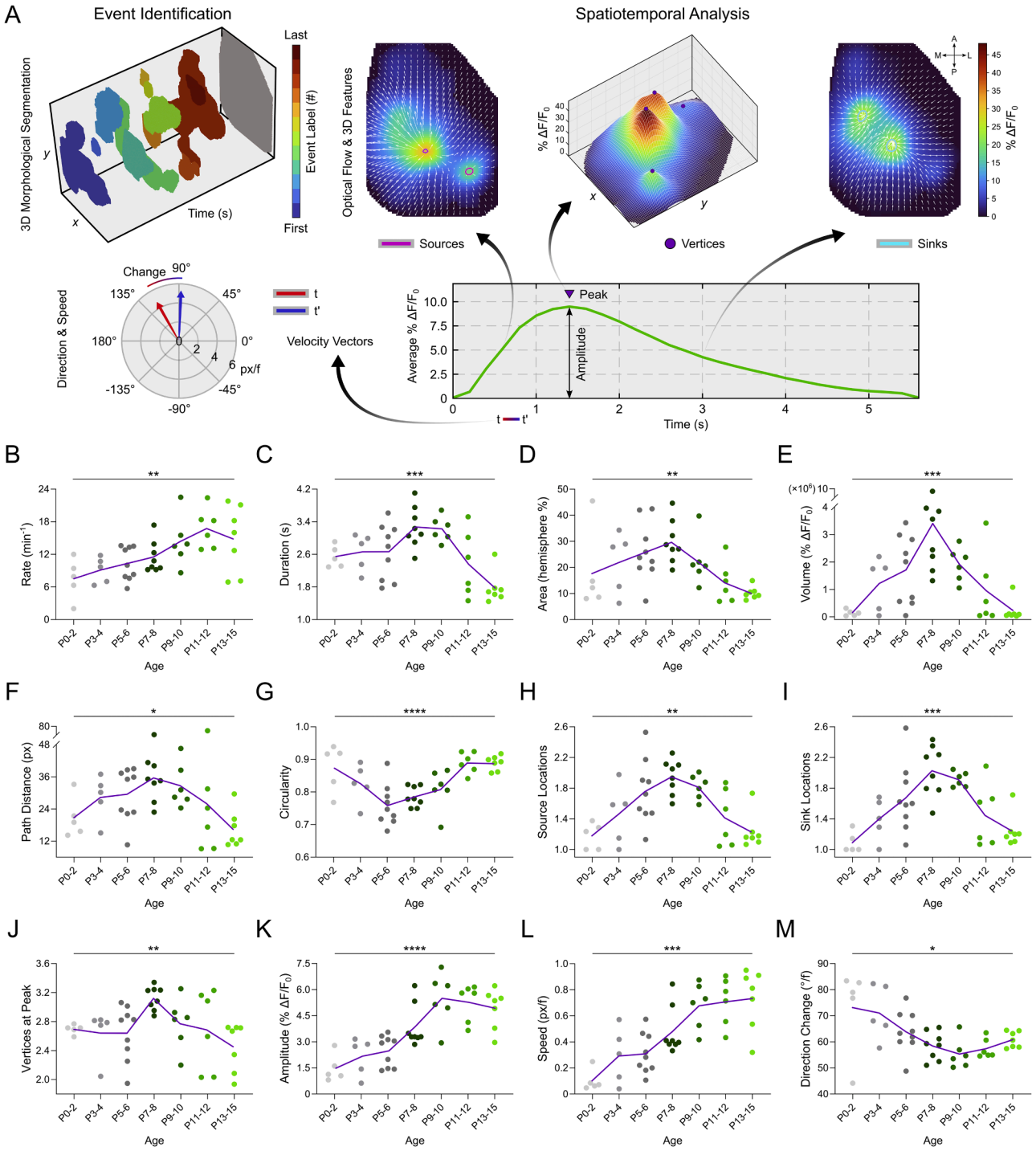

Fig. 3. Spatiotemporal characterization of mesoscale calcium dynamics. (**A**) Graphical scheme of the analysis pipeline. After identifying calcium events through 3D morphological segmentation (top-left), multiple features are extracted based on event kinetic (bottom-right), geometry and optical flow methods (top-right). Through the latter, velocity vectors describing signal speed and direction are computed for each frame (bottom-left). (B–M) Spatiotemporal properties of calcium events over postnatal development. Besides the rate of occurrence during the recording time (**B**), the following average parameters are computed to characterize the magnitude, morphology, location, and motion of events: duration (**C**), total area (**D**), cumulative volume (**E**), traveled distance (**F**), average circularity (**G**), number of independent locations across the hemisphere of sources (**H**) and sinks (**I**), number of vertices at the temporal peak (**J**), peak amplitude (**K**), average instantaneous speed (**L**), and average angle difference between consecutive velocity vectors (**M**) . Dot plots represent average values per animal, whereas lines (purple) indicate the age group mean. $*p < 0.05$, $**p < 0.01$, $***p < 0.001$, $****p < 0.0001$, one-way ANOVA or Kruskal-Wallis test.

maturation of neural networks and feeds back on the spatiotemporal properties of spontaneous activity (Nakazawa et al., 2020). To characterize these at the mesoscopic level, we performed a three-dimensional morphological segmentation of significant $\Delta F/F_0$ fluctuations (Fig. 3**A**). This procedure yielded a good separation of calcium transients, with the majority of them displaying a single temporal peak and a restricted temporal overlap (**Fig. S4A, B**). To describe the features of these complex events, we then combined the analysis of kinetic and geometric properties with optical flow methods (**Video S10**). In particular, the latter enabled the estimation of velocity vector fields from image sequences and thus the description of the motion of calcium waves, as well as of their sources and sinks.

The analysis showed that while calcium events became steadily more frequent until P11–12 (Fig. 3**B**, 16.75 ± 3.65 vs 7.52 ± 3.73 min^{-1} at P0–2, $p = 0.0073$, Tukey's multiple comparisons test), their duration peaked at P7–8 and then decreased (Fig. 3**C**, 3.27 ± 0.51 vs 1.77 ± 0.38 s at P13–15, $p = 0.0011$, Dunn's multiple comparisons test). At the end of the first postnatal week, events not only lasted longer, but also involved a larger fraction of the hemisphere (Fig. 3**D**, 29.88 ± 8.25 at P7–8 vs 10.19 ± 2.38 % at P13–15, $p = 0.0112$, Dunn's multiple comparisons test), resulting in an overall stronger activation as shown by the quantification of the total volume (Fig. 3**E**, $3.4 \times 10^6 \pm 2.2 \times 10^6$ at P7–8 vs $2.2 \times 10^5 \pm 3.8 \times 10^5$ % $\Delta F/F_0$ at P13–15, $p = 0.002$, Dunn's multiple comparisons test). Moreover, events towards the end of the first postnatal week spread farther across the hemisphere (Fig. 3**F**, 35.64 ± 8.76 at P7–8 vs 16.33 ± 6.87 pixels at P13–15, $p = 0.0226$, Tukey's multiple comparisons test) and were characterized by a more complex shape, as suggested by the lower circularity descriptor (Fig. 3**G**, 0.76 ± 0.06 at P5–6 vs 0.89 ± 0.02 at P13–15, $p = 0.0002$, Tukey's multiple comparisons test). Scaling back and converting the values according to the actual cortical size (in mm) confirmed the observed developmental change in events' area and distance, excluding tissue growth as its causing factor (**Fig. S4C, D**).

The optical flow properties of calcium waves were characterized with a consolidated algorithm (Afrashteh et al., 2017) after optimizing its main parameter (α) to enable source and sink detection on the lowest SNR age group P0–2 (**Fig. S4E, F**). In line with the more extended and complex morphology, the average number of source and sink locations per event was high at the end of the first postnatal week and then progressively decreased (Fig. 3**H**, 1.95 ± 0.22 at P7–8 vs 1.23 ± 0.23 at P13–15, $p = 0.0129$; Fig. 3**I**, 2.03 ± 0.33 at P7–8 vs 1.24 ± 0.21 at P13–15, $p = 0.0272$, both Dunn's multiple comparisons test). In addition, sources and sinks tended to localize close to each other across all postnatal stages, indicating a mainly vertical diffusion of the signal (**Fig. S4G**). Similarly, the number of vertices detected at the peak time reached its maximum at P7–8 and then reduced (Fig. 3**J**, 3.12 ± 0.16 vs 2.45 ± 0.33 at P13–15, $p = 0.0033$, Dunn's multiple comparisons test). The amplitude of the peak instead gradually increased, reaching a plateau at P9–10 (Fig. 3**K**, 5.49 ± 1.51 vs 1.48 ± 0.79 % $\Delta F/F_0$ at P0–2, $p = 0.0047$, Dunn's multiple comparisons test). Accordingly, the wave speed, computed as the average magnitude of the instantaneous velocity vectors, peaked at the end of the second postnatal week (Fig. 3**L**, from 0.1 ± 0.08 at P0–2 to 0.74 ± 0.23 pixel per frame at P13–15, $p = 0.0021$, Dunn's multiple comparisons test). The same developmental trend was retained when accounting for differences in hemispheric size and expressing the speed in units of mm/s (**Fig. S4H**). Conversely, the motion directionality became more stable, as quantified by the progressively smaller angle difference between consecutive instantaneous velocity vectors (Fig. 3**M**, 66.72 ± 11.11 at P0–7, $n = 23$, vs 57.95 ± 4.74° per frame at P8–15, $n = 23$, $p = 0.0011$, Student unpaired *t*-test).

Altogether the spatiotemporal analysis of mesoscale cortical dynamics highlights a marked developmental change in the properties of calcium transients. During the first postnatal week, calcium events feature strong activations and synchronized broad areas of the cortex, thus reflecting early bursting activity. Later on, when neural activity becomes sparser, shorter calcium waves propagate faster and more stably, suggesting a more efficient information transfer across the cortex.

3.4. Cortical calcium waves undergo a topographic transition within the first two postnatal weeks

The mature cerebral cortex presents a defined topographic organization, largely tethering the structure with function of cortical regions (Mohajerani et al., 2013). We thus investigated if and how early calcium dynamics correlated with the emergence of canonical topographic domains of the mature cortex and/or with their functional interactions. To this end, we analyzed spontaneous activity features with its spatial relation to prospective functional areas delineated from the atlas of the adult mouse cortex (Lau et al., 2008). In particular, we employed a reference map, which broadly encompasses the main sensory and motor regions, as well as the main associative areas (Fig. 4**A**, left). Although, especially at early developmental stages, functional inputs and intracortical connections are yet to be formed, which leads to uncertainty in the delineation of cortical regions, this approach allows to characterize the distribution of activity across the cortical hemisphere over postnatal development in a referenceable manner (Fig. 4**A**, middle).

We first superimposed the reference map onto the average cumulative $\Delta F/F_0$ projections of the hemisphere at the different age groups to evaluate general activity levels in cortical areas (Fig. 4**B**). In detail, while at P0–2 the cumulative calcium signal was more homogeneously distributed across the hemisphere, from P3 to P6 it appeared concentrated within the retrosplenial cortex (Rsp). From P7 to P10, the posterior parietal cortex (PPC) showed the highest intensity, whereas from P11–12, just before eye opening, activity localized mainly in the visual cortex (Vis). To quantify activity parameters and provide developmental trajectories of cortical areas, we computed basic features from average significant $\Delta F/F_0$ fluctuations and assigned the previously identified event markers to each region (Fig. 4**A**, middle). In addition, we also calculated average region values for multiple other parameters sampled at the pixel level (**Fig. S5**). The analysis showed that activity levels in different cortical regions presented common developmental trends, as quantified by the active time and the inter-active time (Fig. 4**C, D**, no interaction between age groups and cortical regions, $F(54, 390) = 0.6366$, $p = 0.98$ and $F(54, 387) = 1.097$, $p = 0.31$, respectively, two-way ANOVA). In detail, the active time trajectories peaked between P7 and P10, and then decreased (age group factor, $F(6, 390) = 50.13$, $p < 0.0001$, two-way ANOVA), whereas the inter-active time reached a minimum around P7–10 across all regions (age group factor, $F(6, 387) = 15.09$, $p < 0.0001$, two-way ANOVA). Taken together, these two observations indicated that activity bouts within cortical regions became gradually shorter during the second postnatal week. This applies in particular to the somato-motor regions, which also displayed higher peak frequencies in their calcium signals as compared to caudal regions (**Fig. S5A**). The developmental trajectories of signal intensity and area fraction displayed instead more variable trends across cortical regions (Fig. 4**E, F**, interaction between age groups and cortical regions, $F(54, 388) = 3.189$, $p < 0.0001$ and $F(54, 388) = 2.128$, $p < 0.0001$, respectively, two-way ANOVA). During the first postnatal week, the Rsp and PPC showed the strongest intensity (e.g. at P3–4, Rsp 33.27 ± 14.91 vs SSb 15.56 ± 10.17 % $\Delta F/F_0$, $p = 0.0008$, and PPC 25.88 ± 16.48 vs MOs 9.68 ± 6.57 % $\Delta F/F_0$, $p = 0.0037$, Tukey's multiple comparisons test) and a wider activation extension (e.g. at P5–6, Rsp 82.92 ± 6.64 vs Vis 46.52 ± 14.83 % of area, $p < 0.0001$, and PPC 81.29 ± 21.73 vs SSb 53.21 ± 19.91 % of area, $p = 0.0028$, Tukey's multiple comparisons test), whereas later on, all trajectories converged to similar values (ns differences at P13–15, Tukey's multiple comparisons test). These observations were corroborated by the quantification of event features in the different cortical regions. The overall event rate (Fig. 4**G**) showed similar developmental trends across cortical regions (age group factor, $F(6, 390) = 35.64$, $p < 0.0001$, two-way ANOVA) and maintained roughly the same relationships (no interaction between age groups and cortical

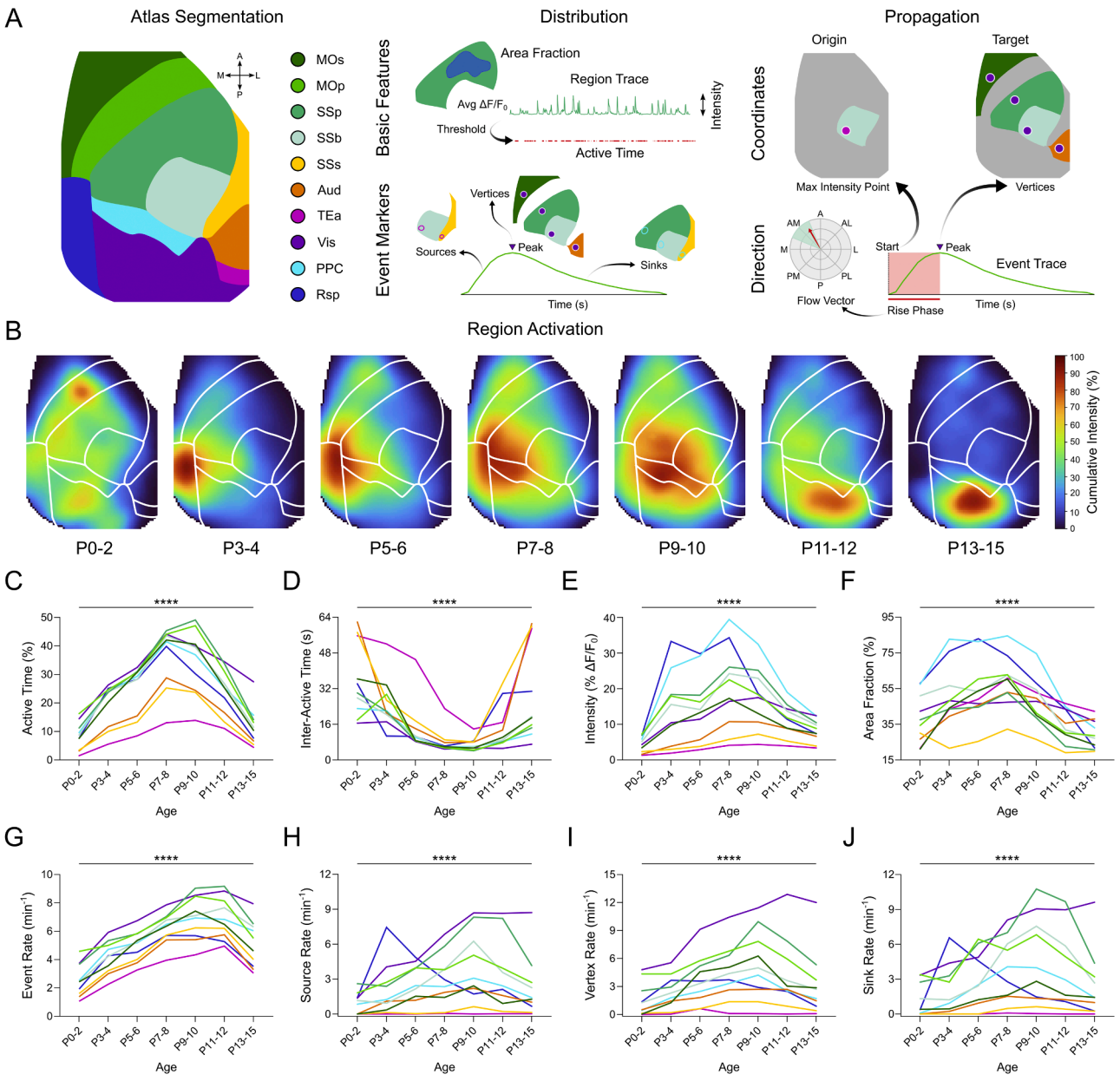

Fig. 4. Distribution of activity levels across cortical regions. (**A**) Atlas-based segmentation of the right cortical hemisphere (left). The following regions of the cortex are outlined: secondary motor (MOs, dark green), primary motor (MOp, light green), primary somatosensory (SSp, sea green), barrel somatosensory (SSb, turquoise), secondary somatosensory (SSs, yellow), auditory (Aud, orange), temporal association (TEa, magenta), visual (Vis, purple), posterior parietal (PPC, cyan), and retrosplenial (Rsp, blue). Starting from these, average $\Delta F/F_0$ traces are computed and, based on their significant fluctuations, basic activity features are extracted (center-top). Leveraging the event-based and optical flow parameters, activity distribution (center-bottom) and propagation patterns (right) are characterized. (**B**) Outlines of cortical regions are overlaid onto average cumulative intensity projections of hemispheric activity. (C–F) Quantification of basic region features across postnatal development. The active time (**C**) is quantified as the relative fraction of recording time with significant fluctuations. Conversely, the average duration of sub-threshold segments is computed as the inter-active time (**D**). Signal intensity (**E**) is quantified as the maximum average value for each region trace, whereas area fraction (**F**) is the average active portion of region during active frames. (G–J) Quantification of event markers in cortical regions across postnatal development. Event rate (**G**) is computed as the number of events, which engage each region during the recording time. The 3D indices of sources (**H**), vertices (**I**), and sinks (**J**) are sorted into the different cortical regions and their frequency over the recording time is calculated. Colored lines indicate average values per age group. ****$p < 0.0001$ main effects of two-way ANOVA.

regions, F(54, 390) = 0.3786, $p = 0.99$, two-way ANOVA). The latter partly reflected spatial constrains such as size and relative position of areas within the hemisphere. Similar regional differences were also observed in further average properties, such as entropy, correlation, and parcellation (**Fig. S5B–D**). The quantification of sources, vertices, and sinks within different cortical regions highlighted instead more diversified developmental trends (Fig. 4**H–J**, interaction between age groups and cortical regions, F(54, 390) = 2.723, $p < 0.0001$, F(54, 390) = 1.576, $p = 0.0084$, and F (54, 390) = 1.940, $p = 0.0002$, respectively, two-way ANOVA). The Rsp largely contributed to the emergence of spontaneous activity in the cortex during the first postnatal week, being its primary source at P3–4 (Fig. 4**H**, e.g. Rsp 7.44 ± 3.63 vs SSb 0.92 ± 0.78 min^{-1}, $p < 0.0001$, Tukey's multiple comparisons test). Subsequently the source rate in Rsp gradually decreased, while the primary somatosensory cortex (SSp) and Vis became the main drivers of activity from P7–8 onwards (e.g. at P7–8, SSp 5.83 ± 2.74 vs MOs 1.43 ± 1.62

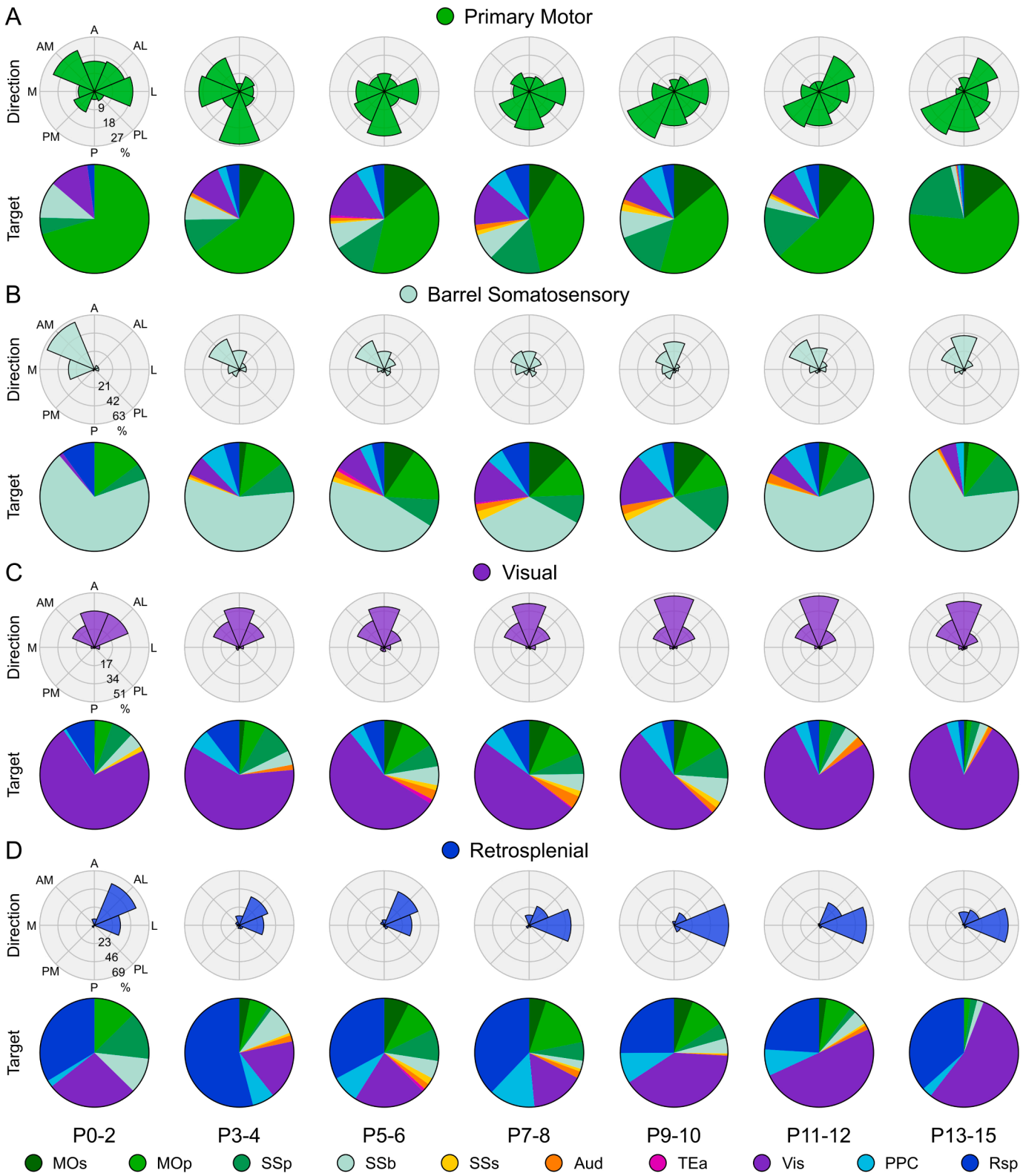

Fig. 5. Calcium waves propagation throughout the cortical hemisphere. Direction and target of calcium waves across development are presented respectively as average polar histograms (top graphs in each panel) and average pie charts (bottom graphs in each panel) for each age group. After sorting calcium events based on their origin in the different cortical regions, direction histograms are obtained by binning the event rise phase flow vectors in the following eight polar coordinates (see also Fig. 4A, right): lateral (L), antero-lateral (AL), anterior (A), antero-medial (AM), medial (M), postero-medial (PM), posterior (P), and postero-lateral (PL). For pie charts, vertices coordinates are assigned to the respective target regions and the resulting proportions are color-coded (see also Fig. 4A, left). Results are shown for primary motor (**A**), barrel somatosensory (**B**), visual (**C**), and retrosplenial (**D**) cortex.

min^{-1}, $p = 0.0011$, and at P13–15, Vis 8.71 ± 3.29 vs SSb 2.26 ± 2.58 min^{-1}, $p < 0.0001$, Tukey's multiple comparisons test). The Vis displayed not only the highest level of sources at the end of the second postnatal week, but also the highest rate of vertices throughout development (Fig. 4**I**). This suggests a high degree of participation of the Vis in events arising from other regions, but also a higher parcellation level (**Fig. S5D**). Sink rates displayed comparable trends to sources (Fig. 4**J**), reflecting the dominant columnar organization of the cortex.

Next, we investigated how activity propagated across cortical regions, analyzing the flow direction and targets of calcium waves. Flow direction was determined by summing the velocity vectors limited to the rise phase of the event and by binning its outcome along the eight primary polar coordinates (see graphical scheme in Fig. 4**A**, right). Indeed, the event decay phase, besides reflecting mainly the slow and possibly noisy kinetic of the sensor, tends to generate vector fields of opposite directions compared to the rise phase, thus canceling each other out (Townsend and Gong, 2018). The targets of calcium waves were defined based on the location of the vertices at the peak time, which, depending on the event complexity, could be also distributed across several regions. Based on the preceding results of activity distribution, we focused our attention on the following cortical regions: primary motor cortex (MOp), barrel somatosensory cortex (SSb), Vis, and Rsp. The remaining regions are reported in **Fig. S6**.

The analysis showed that starting from P3–4 the majority of events originating in the MOp propagated mainly in the posterior quadrants, with either the posterior (P) or the postero-medial (PM) bin representing the average largest direction (Fig. 5**A**, between P3 and P15, P 19.79 ± 13.86 %, and PM 18.25 ± 12.8 %, $n = 40$, $Q = 46.93$, $p < 0.0001$, Friedman test). In addition, events from MOp either remained localized within the region boundaries (P0–15, 49.6 ± 20.1 %, $n = 45$, $Q = 277.9$, $p < 0.0001$, Friedman test) or targeted predominantly SSp (13.84 ± 6.58 %) or the secondary motor cortex (MOs 10.52 ± 10.25 %). Conversely, the largest fraction of events arising from the SSb (Fig. 5**B**) traveled in the anterior (P0–15, A 24.08 ± 20.55 %, $n = 45$, $Q = 126.3$, $p < 0.0001$, Friedman test) or antero-medial (AM 33.2 ± 24.33 %) direction throughout the first two postnatal weeks, and outside its borders reached especially MOp (11.86 ± 8.34 %, $n = 45$, $Q = 253.6$, $p < 0.0001$, Friedman test) and SSp (9.71 ± 7.84 %). Among the caudal parts of the hemisphere, calcium waves from the Vis moved almost exclusively frontally (Fig. 5**C**, P0–15, AM+A+AL 86.68 ± 7.09 %, $n = 46$, $Q = 251.8$, $p < 0.0001$, Friedman test) and presented more heterogeneous external targets (e.g. P0–15, MOp 7.7 ± 5.89, SSp 6.3 ± 5.15, SSb 4.85 ± 4.59, and Rsp 6.01 ± 4.34 %, $n = 46$, $Q = 238.4$, $p < 0.0001$, Friedman test). Of note, at P13–15 the vast majority (85.86 ± 14.47 %, $n = 7$, $Q = 35.66$, $p < 0.0001$, Friedman test) of event remained localized within the Vis. Finally, activity driven by the Rsp (Fig. 5**D**) spread predominantly antero-laterally (AL) until P6 (46.51 ± 21.68 %, $n = 18$, $Q = 87.86$, $p < 0.0001$, Friedman test) and in the lateral (L) direction from P7 (58.86 ± 29.47 %, $n = 25$, $Q = 104.1$, $p < 0.0001$, Friedman test). Interestingly, a larger proportion of targets was localized outside the Rsp margins, preferentially within the somato-motor regions (MOs, MOp, SSp, SSb) until P8 (pooled data at P0–8, 29.95 ± 13.49 vs Vis 19.85 ±

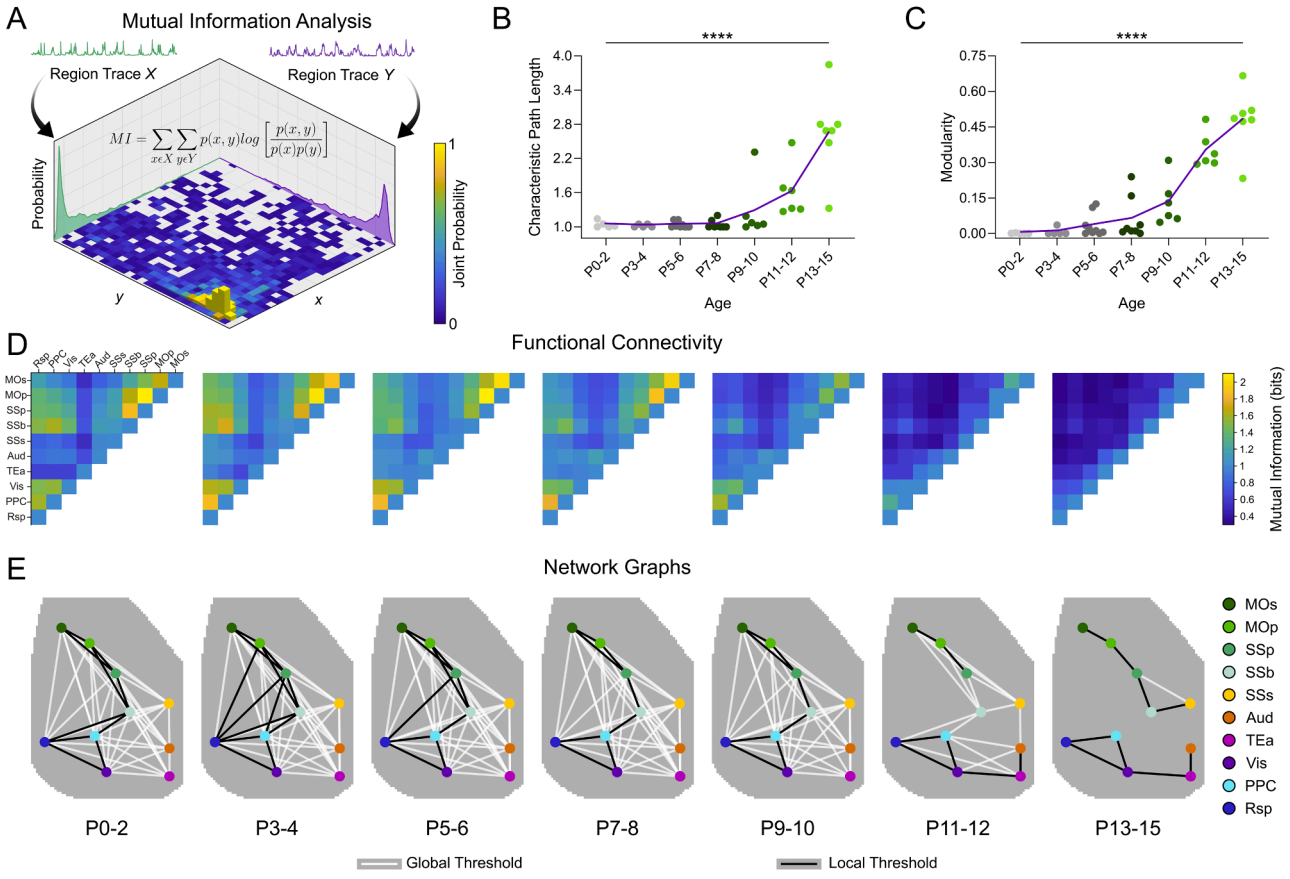

Fig. 6. Functional connectivity within developing cortical networks. (**A**) Pairwise undirected connectivity is defined based on mutual information between region calcium traces. After testing for statistical significance and matrix thresholding, network graphs, where nodes represent cortical regions and edges their long-range connections, are constructed. Graph properties describing network topology of individual networks, namely characteristic path length (**B**) and modularity (**C**), are compared across development using a global threshold. Dot plots represent individual experiments, whereas lines (purple) indicate the age group mean. ****$p <$ 0.0001, Kruskal-Wallis test. (**D**) Average connectivity matrices per each age group are presented and color-coded according to their mutual information values. (**E**) Representative network graphs are constructed based on significant connections between nodes (color-coded centroids of cortical regions), using either a global (white lines) or a local (black lines) threshold.

10.35 %, $n = 26$, $p = 0.0009$, Student paired t-test) and later on within the Vis (P9–15, 48.12 ± 33.38 %, $n = 17$, $Q = 91.12$, $p < 0.0001$, Friedman test). Although the study of propagation is necessarily constrained by the relative positions of regions across the cortical surface, it should be highlighted that the SSb, while being roughly located in the middle of the hemisphere, was characterized by events consistently propagating towards the anterior sectors. Moreover, the predominant localization of targets within each region boundaries further corroborates the characterization of mesoscale calcium events, as columnar burst of activity with limited horizontal spread over the cortical surface. Nonetheless, especially between P5 and P10, large events could also target distant areas, mostly as the result of consecutive activations cascades (see also **Videos S1**–**7** and **10**), likely through long-range horizontal connections or subcortical pathways.

Overall, our results indicate that the Rsp generates strong and uniform calcium elevations during the first postnatal week, whereas later on activity arises mainly in the sensory cortices leading to confined and complex activity patterns in the Vis at the end of the second postnatal week. In general, calcium waves propagate along plastic, yet defined directions across different developmental stages, suggesting the emergence and refinement of preferential connectivity profiles within the cortex.

3.5. Spontaneous activity reflects the establishment of cortical network connectivity

To generate higher-order cognitive states, information from local cortical regions must be integrated in an ordered and hierarchical manner, giving rise to a defined functional network architecture (Meunier et al., 2009). In the mature brain, the latter is maintained even in the absence of tasks or sensory stimuli and requires long-range connectivity profiles (Deco et al., 2013). We thus investigated if and how spontaneous activity reflects the development of the cortex functional organization, by reconstructing the network connectivity and its topology through graph theory.

To this end, we computed pairwise relationships of average region $\Delta F/F_0$ traces using mutual information (Fig. 6**A**), an information theory measure which enables the description of nonlinear interaction between variables. Employing this metric, we obtained undirected connectivity matrices and constructed individual and age group networks, to respectively quantify the developing network topology and characterize average connectivity profiles. To compare graph attributes across different developmental stages, we adopted a global threshold, which avoided the generation of unconnected networks. The analysis showed that during the first postnatal week the high connectivity degree and strength (**Fig. S7A, B**) led to a high level of integration across cortical regions as confirmed by the low characteristic path length until P7–8 (Fig. 6**B**, 1.04 ± 0.08 at P7–8 vs 2.66 ± 0.74 at P13–15, $p = 0.0012$, Dunn's multiple comparisons test). Conversely, during the second postnatal week the clustering coefficient of cortical networks dropped (**Fig. S7C**), indicating a strongly segregated organization, as quantified by the high modularity index (Fig. 6**C**, 0.48 ± 0.13 at P13–15 as compared to $6 \times 10^{-4} \pm 1.3 \times 10^{-3}$ at P0–2, $p = 0.0003$, Dunn's multiple comparisons test). Network connectivity profiles were then characterized starting from average mutual information matrices (Fig. 6**D**). Comparing graphs across development highlighted initially high and then sparsely connected networks (Fig. 6**E**, white lines). Significant connections within each age group were instead visualized by applying a local threshold (black lines). Overall, network graphs revealed the presence of a somato-motor subnetwork (i.e. strong connections between MOs, MOp, SSp, and SSb) already after birth, and a high degree of connectivity between the Rsp and multiple other regions until P5–6. Note, also in this regard the high values of mutual information in the relative connectivity matrices. Subsequently, a distinct caudal subnetwork emerged at P11–12, whose structure, in parallel to the somato-motor one, consolidated at P13–15. Thus, at the second postnatal week, the identified functional organization resembled canonical subnetworks present in the adult mouse cortex (Zingg et al., 2014). Interestingly, such long-range network architecture was only partially recapitulated by the linear relationships between different cortical regions computed via Pearson correlation (**Fig. S7D, E**).

The observed segregation of cortical networks indicated the presence of distinct modules, which are topological entities characterized by a high degree of connectivity between their nodes and sparse connections with nodes belonging to other modules. To test this, we reconstructed network connectivity at a lower order of magnitude, by tiling each cortical region into evenly spaced patches (**Fig. S7F**). To emphasize difference across modules, an individual network threshold was applied. The analysis showed that while all modules reached a high clustering coefficient (**Fig. S7G**), their inner characteristic path length converged to low values during the second postnatal week (**Fig. S7H**), indicating a highly efficient communication within each region.

In conclusion, functional connectivity analysis of the cortex at the macroscale highlights long-range interactions, which disclose the early presence of a somato-motor subnetwork and the subsequent emergence of a caudal one. The resulting network topology culminates in a highly modular architecture at the end of the second postnatal week, enabling functional segregation of cortical regions and ordered hierarchical integration of information.

4. Discussion

Early neural activity contributes to the development of the cerebral cortex at different scales, from regulating the number and identity of neurons to impinging on the cytoarchitecture and topography of local networks (Cossart and Garel, 2022; Luhmann et al., 2016; Martini et al., 2021). Here, we recorded spontaneous mesoscale calcium dynamics across postnatal mouse development, and investigated their correlation with the maturation of the cortical functional architecture. We showed that: 1) Wide-field fluorescence imaging in GCaMP6s transgenic mice closely reflects the electrophysiological maturation of neuronal populations across fine stages of development; 2) Functional domains of the cortex steadily refine based on a primordial macroscopic organization of the cortical hemisphere; 3) Mesoscale neural dynamics transition from large and widespread events during the first postnatal week to swift waves in the second postnatal week; 4) The levels of activity mature rather uniformly across the hemisphere, but its features show significant topographic differences; 5) Functional connectivity profiles of the cortex reveal the gradual segregation of an early somato-motor from a caudal subnetwork and the emergence of a highly modular network topology at the end of the second postnatal week. Overall, our findings highlight that mesoscale calcium dynamics can be instructive for the proper development of the functional architecture of the cortex.

During the perinatal period, the cerebral cortex exhibits diverse neural dynamics that are modulated by peripheral inputs, central pattern generators, and by the maturation of sensory modalities (Leighton and Lohmann, 2016; Yang et al., 2016). To investigate large-scale interactions of spontaneous activity across the entire right cortical hemisphere, we employed wide-field fluorescence imaging on transgenic mice that widely expressed the GCaMP6s indicator in neuronal populations (Madisen et al., 2015). Leveraging the high signal-to-noise ratio of this calcium sensor (Chen et al., 2013), we could monitor cortical dynamics in a minimally invasive manner and characterized developmental changes at a fine temporal scale. At the same time, calcium recordings in the present study were performed in mouse pups under mild urethane anesthesia, whose impact on neural activity should not be neglected. Urethane has been proven as the most suitable anesthetic for long recordings of spontaneous electrical activity with minimal effects on neuronal discharge patterns, cortico-subcortical interactions, and functional connectivity (Chini et al., 2019; Paasonen et al., 2018; Shumkova et al., 2021). Accordingly, we have previously shown that despite slightly diminished event frequency and spectral

power, regional differences in early cortical activity were preserved under low dose urethane anesthesia (Blanquie et al., 2017). While these evidences suggest a high correspondence between urethane anesthesia and awake state, precautions should be taken when extrapolating our results. Moreover, pan-neuronal overexpression of GCaMP6s introduces increased calcium buffering, which can potentially influence the kinetics and propagation of calcium waves. However, in line with previous studies (Madisen et al., 2015; Steinmetz et al., 2017), no aberrant neuronal activity was recorded from postnatal Snap25–2A-GCaMP6s-D mice. In our study, we observed a progressive increase in the relative intensity of the fluorescent signal during the first postnatal week. Especially with genetically encoded calcium indicators, high amplitude calcium elevations result from the temporal integration of action potential bursts (Inoue, 2021) and are in accordance with high-frequency oscillations recorded in electrophysiological studies at this young age (Yang et al., 2009). Subsequently, when neuronal activity becomes sparse and uncorrelated during the second postnatal week (Rochefort et al., 2009), the fluorescence intensity declined together with an increase in signal frequency and entropy. While the former reflected a higher rate of calcium oscillations (Uhlén, 2004), the latter described the number of different states present in a signal (Timme and Lapish, 2018) and thus revealed a higher information content of neuronal activity.

The functional activation of the mature cortex at rest displays a defined spatial organization that is highly conserved across individuals (Damoiseaux et al., 2006; Grandjean et al., 2020). Classically, domains with similar function have been derived by analyzing the temporal correlations of neural signals across the cortical surface (Deco and Corbetta, 2010; Leopold and Maier, 2012), prompting the characterization of main subnetworks (Glasser et al., 2016; Zingg et al., 2014). Here, we show that a macroscopic organization of the cortex is already present shortly after birth, and is maintained throughout postnatal development. In detail, while the calcium signal across the hemisphere progressively decorrelated, two main blocks could be delineated: a posterior domain covering most of the occipital and parietal cortex, and a fronto-lateral one oriented along the antero-lateral axis. Interestingly, this peculiar configuration has been previously observed in the adult mouse using both wide-field optical imaging and fMRI (Benisty et al., 2023; Vafaii et al., 2024), and resonates with studies describing expression patterns of morphogens (O'Leary et al., 2007), and virtual tractography of the cortex (Oh et al., 2014). Combined, these evidences suggest that a primordial genetic program might prime the macroscopic organization of the cortical hemisphere recorded as early as P0 in this study. Within this framework, increasing cortical parcels arose with further development and displayed refined territories. This adheres to a well-described gain in the complexity of neural dynamics, but also reflects the gradual divergence of spontaneous activity, from solely providing a template for sensory driven experience, as seen during active sleep in infant rodents (Del Rio-Bermudez et al., 2020; McVea et al., 2012), to encoding more complex representations when exploratory behavior starts (Avitan and Stringer, 2022). Thus, our findings suggest that linear dependences of wide-field signals retain both large-scale and local interactions after birth, with the former likely depending on biologically predetermined aspects and the latter reflecting the development of their respective anatomical correlates.

The territories of cortical parcels are gradually shaped and feed back onto neural oscillations (Luhmann and Khazipov, 2018), which can be recorded as complex spatiotemporal network dynamics via wide-field calcium imaging in vivo (Ren and Komiyama, 2021). To characterize the latter, we designed a multi-parameter analysis combining common mathematical approaches with optical flow methods (Afrashteh et al., 2017; Townsend and Gong, 2018). During the first postnatal week, mesoscale calcium events became gradually larger, with a broad extension and multiple sources across almost the entire hemisphere. This is in accordance to sleep-related large-scale waves described at the end of the first postnatal week in another transgenic mouse line for GCaMP6s in the brain (Tabuena et al., 2022), and reflects large neuronal discharges observed in the rodent cortex with voltage-sensitive dye imaging (Chan et al., 2015) and multi-unit recordings (Luhmann, 2016). Subsequently, events not only became shorter and confined, but also their motion was faster and their directionality more stable. Here, it should be considered that, although neurovascular coupling is not yet fully developed in the mouse brain until the end of the second postnatal week (Kozberg et al., 2016), hemoglobin absorption cannot be certainly disentangled from the calcium signal in single-wavelength recordings (Valley et al., 2020), and thus a minor hemodynamic contamination on the temporal properties of calcium transients cannot be excluded. In addition, group-wise comparisons across age spans of 2 to 3 consecutive postnatal days can well capture gradual transitions, but at the same time might hamper the identification of more subtle differences between contiguous time points. Nevertheless, the developmental changes in calcium event features and the resulting inflection point between the first and second postnatal week in our analysis are in line with the developmentally critical period and the sparsification of neuronal activity (Colonnese et al., 2010). The precise etiology of early large oscillations and their sudden transition to sparse activity are still under investigation (Wu et al., 2024). However, recent evidences point at the maturation of GABAergic interneurons as a key factor (Mòdol et al., 2024). Moreover, the maturation of synaptic and electrophysiological properties of cortical neurons (Etherington and Williams, 2011; Nakazawa et al., 2020) likely attributes to the observed refinement of calcium signal kinetics and, thus, to a more reliable communication and more efficient information transfer between distant areas of the cortex.

Parallel to the described network state transition, spontaneous activity patterns display regional differences that depend on incoming inputs and/or neuronal circuit topography (Nakazawa and Iwasato, 2021). However, local activity patterns are spatiotemporally integrated in mesoscale calcium dynamics, commonly leading to broad activations across the cortical hemisphere. Thus, we used an anatomical atlas, outlining the main functional regions of the adult cortex, to investigate the overall distribution of mesoscale dynamics within and across cortical areas and to infer regional developmental trends. Although we confirmed the anatomical segmentation by sensory stimulations in later age groups, this mapping approach must be considered with care as primary functional regions and association cortices likely do not grow proportionally, which makes their precise delimitation uncertain. However, gross anatomical annotations can provide a referenceable map for future studies and highlight noteworthy regional differences in a straightforward manner. Notably, we observed a prominent role of the retrosplenial cortex (Rsp) during the first postnatal week. In line with similar findings in P3 mice (Mojtahedi et al., 2021), Rsp displayed high-intensity events engaging multiple other regions between P0 and P6, and a preferential interaction with the visual cortex (Vis) from P7 onwards. Rsp is a highly interconnected associative area (Vann et al., 2009), that has been implicated in different cognitive roles, such as spatial navigation and visuospatial integration (Mitchell et al., 2018), or as part of the default-mode network in the brain at rest (Stafford et al., 2014). Thus, the high activity levels we observed in Rsp corroborate the early emergence of its long-range functional connections (Mojtahedi et al., 2021). On the other hand, the differential interactions with cortical regions might reflect the staggered development of networks that support its diverse cognitive functions. During the second postnatal week, spontaneous activity predominantly originated in the primary somatosensory cortex first and then, from P11 onwards, in the Vis. In particular, spontaneous activity in the latter was characterized by confined events and by a high number of cortical parcels right before eye opening. Although the topographic organization of the mouse Vis is not as evident as in other mammals (Kaschube, 2014), the detected features likely reflect its highly patchy structure (Ji et al., 2015). Here, it should be noted that differences between annotated anatomical regions can be biased by heterogeneity in their cell density and layer organization (Waters, 2020), as well as by their different topographic positions in respect to the imaging field and angle (Cardin et al., 2020).

Nevertheless, the results indicate that spontaneous activity is prevalent and highly structured especially in the sensory cortices, which already early in development receive thalamic inputs (Moreno-Juan et al., 2017) and display columnar activation patterns (Kummer et al., 2016).

Spontaneous mesoscale dynamics manifested predominantly as focal cortical activations, with local horizontal spread or as activation cascades engaging also more distant parts of the cortex. Taking this into account, we characterized the propagation of calcium waves within preferential interaction pathways, for example between the barrel somatosensory and motor cortices or between Rsp and Vis. Lastly, we reconstructed functional connections and the overall network structure, through the analysis of the statistical dependencies between region traces. Cortical connectivity profiles can be affected by methodically hidden, nonlinear dynamics between cortical regions through deep-layer connections or subcortical nuclei (Hirsch and Wohlschlaeger, 2023). Accordingly, as opposed to pure linear correlation, mutual information appeared to better capture long-range connections similar to other studies (Zhang et al., 2018). In particular, our analysis revealed canonical pathways of connectivity, confirming the early presence of a somato-motor network (Cross et al., 2021; Gellért et al., 2023), the hub role of Rsp during the first postnatal week (Mojtahedi et al., 2021), and the segregation of a caudal subnetwork at the end of the second postnatal week (Rahn et al., 2022; Zingg et al., 2014). Applying graph theory, we then investigated the ensuing network properties. Our results showed that mesoscopic patches within cortical regions became progressively more interconnected, whereas macroscopic domains, i.e. cortical regions, highly segregated. This reflected the development of a hierarchical cortical organization and, as confirmed by the homonymous community structure descriptor, a highly modular topology, which reached its maximum at the end of the second postnatal week. Interestingly, modular organization of spontaneous activity appears as a common developmental feature across different cortical areas and mammalian species (Powell et al., 2024). Such network configuration facilitates the emergence of coherent activity patterns (Zhigalov et al., 2017) and, in turn, supports the development of local cortical circuits by strengthening synaptic inputs (Okujeni et al., 2017) and fostering neuronal survival rates (Warm et al., 2022a). Interestingly, the emergence of comparable network structures (Omidvarnia et al., 2014) and modular topology (Van Den Heuvel et al., 2015) have been observed across perinatal stages of human development, where their presence has been correlated with proper maturation of cognitive functions during childhood (Lei et al., 2024; Li et al., 2024).

The concept of modularity derived from the identification of cortical columns as neurophysiological processing units and has found theoretical support in network neuroscience as a framework to explain the diverse functionality of the cerebral cortex (Stanley et al., 2019). In this context, our results provide new evidences, by showing how early spontaneous mesoscale calcium dynamics reflect both the refinement of the columnar organization of the cortex and the development of a modular functional architecture of the cortex. Pathological alterations of either one can lead to structural abnormalities and to cognitive impairment in the mature cortex (Casanova and Casanova, 2019; Hutsler and Casanova, 2016). This study can thus aid the identification of critical breakpoints during the functional maturation of cortical networks, e.g. in mouse models of autistic syndromes (Sestan and State, 2018), and advance the early diagnosis and therapeutical intervention of neurodevelopmental disorders in human (Luhmann et al., 2022).

Funding

This work was supported by a grant of the Deutsche Forschungsgemeinschaft to H.J.L. and A.S. (CRC1080, project A01).

Ethics statement

All animal experiments conducted in this work were in accordance with national and European laws for the use of animals in research (2010/63/EU) and were approved by the local ethical committee (Landesuntersuchungsamt Rheinland-Pfalz, # 23 177–07/G 20–1–006).

CRediT authorship contribution statement

Davide Warm: Writing – original draft, Writing – review & editing, Visualization, Software, Methodology, Investigation, Formal analysis, Data curation. **Davide Bassetti:** Software, Formal analysis, Data curation. **Levente Gellèrt:** Methodology, Investigation. **Jenq-Wei Yang:** Methodology. **Heiko J. Luhmann:** Writing – review & editing, Supervision, Project administration, Funding acquisition, Conceptualization. **Anne Sinning:** Writing – review & editing, Writing – original draft, Supervision, Project administration, Funding acquisition, Conceptualization, Methodology.

Declaration of competing interest

The authors declare that they have no known competing financial interests or personal relationships that could have appeared to influence the work reported in this paper.

Acknowledgments

We kindly thank Nicole Knauer and Beate Krumm for the excellent technical assistance and David Cabrera-Garcia, Sergei Kirischuk and Werner Kilb for helpful scientific discussions and valuable comments on the manuscript.

Supplementary materials

Supplementary material associated with this article can be found, in the online version, at doi:10.1016/j.neuroimage.2025.121088.

Data availability

Data will be made available on request.

References

Ackman, J.B., Burbridge, T.J., Crair, M.C., 2012. Retinal waves coordinate patterned activity throughout the developing visual system. Nature 490, 219–225. https://doi.org/10.1038/nature11529.

Afrashteh, N., Inayat, S., Mohsenvand, M., Mohajerani, M.H., 2017. Optical-flow analysis toolbox for characterization of spatiotemporal dynamics in mesoscale optical imaging of brain activity. Neuroimage 153, 58–74. https://doi.org/10.1016/j.neuroimage.2017.03.034.

An, S., Kilb, W., Luhmann, H.J., 2014. Sensory-evoked and spontaneous gamma and spindle bursts in neonatal rat motor cortex. J. Neurosci. 34, 10870–10883. https://doi.org/10.1523/jneurosci.4539-13.2014.

Appan, D., Hsu, S.M., Hsu, W.H., Chou, S.J., 2023. Patterning the cerebral cortex into distinct functional domains during development. Curr. Opin. Neurobiol. 80, 102698. https://doi.org/10.1016/j.conb.2023.102698.

Avitan, L., Stringer, C., 2022. Not so spontaneous: multi-dimensional representations of behaviors and context in sensory areas. Neuron 110, 3064–3075. https://doi.org/10.1016/j.neuron.2022.06.019.

Babola, T.A., Li, S., Gribizis, A., Lee, B.J., Issa, J.B., Wang, H.C., Crair, M.C., Bergles, D.E., 2018. Homeostatic control of spontaneous activity in the developing auditory system. Neuron 99, 511–524. https://doi.org/10.1016/j.neuron.2018.07.004 e5.

Benisty, H., Barson, D., Moberly, A.H., Lohani, S., Tang, L., Coifman, R.R., Crair, M.C., Mishne, G., Cardin, J.A., Higley, M.J., 2023. Rapid fluctuations in functional connectivity of cortical networks encode spontaneous behavior. Nat. Neurosci. 27, 148–158. https://doi.org/10.1038/s41593-023-01498-y.

Blanquie, O., Yang, J.W., Kilb, W., Sharopov, S., Sinning, A., Luhmann, H.J., 2017. Electrical activity controls area-specific expression of neuronal apoptosis in the mouse developing cerebral cortex. Elife 6, e27696. https://doi.org/10.7554/elife.27696.

Blumberg, M.S., Dooley, J.C., Tiriac, A., 2022. Sleep, plasticity, and sensory neurodevelopment. Neuron 110, 3230–3242. https://doi.org/10.1016/j.neuron.2022.08.005.

Cadwell, C.R., Bhaduri, A., Mostajo-Radji, M.A., Keefe, M.G., Nowakowski, T.J., 2019. Development and arealization of the cerebral cortex. Neuron 103, 980–1004. https://doi.org/10.1016/j.neuron.2019.07.009.

Cardin, J.A., Crair, M.C., Higley, M.J., 2020. Mesoscopic imaging: shining a wide light on large-scale neural dynamics. Neuron 108, 33–43. https://doi.org/10.1016/j.neuron.2020.09.031.

Casanova, M.F., Casanova, E.L., 2019. The modular organization of the cerebral cortex: evolutionary significance and possible links to neurodevelopmental conditions. J. Comp. Neurol. 527, 1720–1730. https://doi.org/10.1002/cne.24554.

Chan, A.W., Mohajerani, M.H., LeDue, J.M., Wang, Y.T., Murphy, T.H., 2015. Mesoscale infraslow spontaneous membrane potential fluctuations recapitulate high-frequency activity cortical motifs. Nat. Commun. 6, 7738. https://doi.org/10.1038/ncomms8738.

Chen, T.W., Wardill, T.J., Sun, Y., Pulver, S.R., Renninger, S.L., Baohan, A., Schreiter, E. R., Kerr, R.A., Orger, M.B., Jayaraman, V., Looger, L.L., Svoboda, K., Kim, D.S., 2013. Ultrasensitive fluorescent proteins for imaging neuronal activity. Nature 499, 295–300. https://doi.org/10.1038/nature12354.

Chini, M., Gretenkord, S., Kostka, J.K., Pöpplau, J.A., Cornelissen, L., Berde, C.B., Hanganu-Opatz, I.L., Bitzenhofer, S.H., 2019. Neural correlates of anesthesia in newborn mice and humans. Front. Neural Circuits. 13, 451765. https://doi.org/10.3389/fncir.2019.00038.

Colonnese, M., Khazipov, R., 2012. Spontaneous activity in developing sensory circuits: implications for resting state fMRI. Neuroimage 62, 2212–2221. https://doi.org/10.1016/j.neuroimage.2012.02.046.

Colonnese, M.T., Kaminska, A., Minlebaev, M., Milh, M., Bloem, B., Lescure, S., Moriette, G., Chiron, C., Ben-Ari, Y., Khazipov, R., 2010. A conserved switch in sensory processing prepares developing neocortex for vision. Neuron 67, 480–498. https://doi.org/10.1016/j.neuron.2010.07.015.

Cossart, R., Garel, S., 2022. Step by step: cells with multiple functions in cortical circuit assembly. Nat. Rev. Neurosci. 23, 395–410. https://doi.org/10.1038/s41583-022-00585-6.

Cross, C.M., Santos, L.M., Whiteley, N., Luyt, K., Ashby, M.C., 2021. Early functional connectivity in the developing sensorimotor network that is independent of sensory experience. bioRxiv 2021. https://doi.org/10.1101/2021.06.14.448057.

Damoiseaux, J.S., Rombouts, S.A.R.B., Barkhof, F., Scheltens, P., Stam, C.J., Smith, S.M., Beckmann, C.F., 2006. Consistent resting-state networks across healthy subjects. Proc. Natl. Acad. Sci. u S. a 103, 13848–13853. https://doi.org/10.1073/pnas.0601417103.

De Schotten, M.T., Forkel, S.J., 2022. The emergent properties of the connected brain. Science (1979) 378, 505–510. https://doi.org/10.1126/science.abq2591.

Deco, G., Corbetta, M., 2010. The dynamical balance of the brain at rest. Neuroscientist. 17, 107–123. https://doi.org/10.1177/1073858409354384.

Deco, G., Ponce-Alvarez, A., Mantini, D., Romani, G.L., Hagmann, P., Corbetta, M., 2013. Resting-State functional connectivity emerges from structurally and dynamically shaped slow linear fluctuations. J. Neurosci. 33, 11239–11252. https://doi.org/10.1523/jneurosci.1091-13.2013.

Del Rio-Bermudez, C., Kim, J., Sokoloff, G., Blumberg, M.S., 2020. Active sleep promotes coherent oscillatory activity in the cortico-hippocampal system of infant rats. Cereb. Cortex. 30, 2070–2082. https://doi.org/10.1093/cercor/bhz223.

Dooley, J.C., Blumberg, M.S., 2018. Developmental 'awakening' of primary motor cortex to the sensory consequences of movement. Elife 7, e41841. https://doi.org/10.7554/elife.41841.

Erchova, I.A., Lebedev, M.A., Diamond, M.E., 2002. Somatosensory cortical neuronal population activity across states of anaesthesia. Eur. J. Neurosci. 15, 744–752. https://doi.org/10.1046/j.0953-816x.2002.01898.x.

Etherington, S.J., Williams, S.R., 2011. Postnatal development of intrinsic and synaptic properties transforms signaling in the layer 5 excitatory neural network of the visual cortex. J. Neurosci. 31, 9526–9537. https://doi.org/10.1523/jneurosci.0458-11.2011.

Gellért, L., Luhmann, H.J., Kilb, W., 2023. Axonal connections between S1 barrel, M1, and S2 cortex in the newborn mouse. Front. Neuroanat. 17, 1105998. https://doi.org/10.3389/fnana.2023.1105998.

Glanz, R.M., Dooley, J.C., Sokoloff, G., Blumberg, M.S., 2021. Sensory coding of limb kinematics in motor cortex across a key developmental transition. J. Neurosci. 41, 6905–6918. https://doi.org/10.1523/jneurosci.0921-21.2021.

Glasser, M.F., Coalson, T.S., Robinson, E.C., Hacker, C.D., Harwell, J., Yacoub, E., Ugurbil, K., Andersson, J., Beckmann, C.F., Jenkinson, M., Smith, S.M., Van Essen, D. C., 2016. A multi-modal parcellation of human cerebral cortex. Nature 536, 171–178. https://doi.org/10.1038/nature18933.

Grandjean, J., Canella, C., Anckaerts, C., Ayrancı, G., Bougacha, S., Bienert, T., Buehlmann, D., Coletta, L., Gallino, D., Gass, N., Garin, C.M., Nadkarni, N.A., Hübner, N.S., Karatas, M., Komaki, Y., Kreitz, S., Mandino, F., Mechling, A.E., Sato, C., Sauer, K., Shah, D., Strobelt, S., Takata, N., Wank, I., Wu, T., Yahata, N., Yeow, L.Y., Yee, Y., Aoki, I., Chakravarty, M.M., Chang, W.T., Dhenain, M., von Elverfeldt, D., Harsan, L.A., Hess, A., Jiang, T., Keliris, G.A., Lerch, J.P., Meyer-Lindenberg, A., Okano, H., Rudin, M., Sartorius, A., Van der Linden, A., Verhoye, M., Weber-Fahr, W., Wenderoth, N., Zerbi, V., Gozzi, A., 2020. Common functional networks in the mouse brain revealed by multi-centre resting-state fMRI analysis. Neuroimage 205, 116278. https://doi.org/10.1016/j.neuroimage.2019.116278.

Guillamón-Vivancos, T., Aníbal-Martínez, M., Puche-Aroca, L., Moreno-Bravo, J.A., Valdeolmillos, M., Martini, F.J., López-Bendito, G., 2022. Input-dependent segregation of visual and somatosensory circuits in the mouse superior colliculus. Science 377, 845–850. https://doi.org/10.1126/science.abq2960.

Hanganu, I.L., Ben-Ari, Y., Khazipov, R., 2006. Retinal waves trigger spindle bursts in the neonatal rat visual cortex. J. Neurosci. 26, 6728–6736. https://doi.org/10.1523/jneurosci.0752-06.2006.

Henschke, J.U., Oelschlegel, A.M., Angenstein, F., Ohl, F.W., Goldschmidt, J., Kanold, P. O., Budinger, E., 2017. Early sensory experience influences the development of multisensory thalamocortical and intracortical connections of primary sensory cortices. Brain Struct Funct 223, 1165–1190. https://doi.org/10.1007/s00429-017-1549-1.

Hirsch, F., Wohlschlaeger, A., 2023. Subcortical influences on the topology of cortical networks align with functional processing hierarchies. Neuroimage 283, 120417. https://doi.org/10.1016/j.neuroimage.2023.120417.

Hutsler, J.J., Casanova, M.F., 2016. Cortical construction in autism spectrum disorder: columns, connectivity and the subplate. Neuropathol. Appl. Neurobiol. 42, 115–134. https://doi.org/10.1111/nan.12227.

Inoue, M., 2021. Genetically encoded calcium indicators to probe complex brain circuit dynamics in vivo. Neurosci. Res. 169, 2–8. https://doi.org/10.1016/j.neures.2020.05.013.

Ji, W., Gămănuţ, R., Bista, P., D'Souza, R.D., Wang, Q., Burkhalter, A., 2015. Modularity in the organization of mouse primary visual cortex. Neuron 87, 632–643. https://doi.org/10.1016/j.neuron.2015.07.004.

Kaschube, M., 2014. Neural maps versus salt-and-pepper organization in visual cortex. Curr. Opin. Neurobiol. 24, 95–102. https://doi.org/10.1016/j.conb.2013.08.017.

Khazipov, R., Sirota, A., Leinekugel, X., Holmes, G.L., Ben-Ari, Y., Buzsáki, G., 2004. Early motor activity drives spindle bursts in the developing somatosensory cortex. Nature 432, 758–761. https://doi.org/10.1038/nature03132.

Kirkby, L.A., Sack, G.S., Firl, A., Feller, M.B., 2013. A role for correlated spontaneous activity in the assembly of neural circuits. Neuron 80, 1129–1144. https://doi.org/10.1016/j.neuron.2013.10.030.

Kozberg, M.G., Ma, Y., Shaik, M.A., Kim, S.H., Hillman, E.M.C., 2016. Rapid postnatal expansion of neural networks occurs in an environment of altered neurovascular and neurometabolic coupling. J. Neurosci. 36, 6704–6717. https://doi.org/10.1523/jneurosci.2363-15.2016.

Kummer, M., Kirmse, K., Zhang, C., Haueisen, J., Witte, O.W., Holthoff, K., 2016. Column-like Ca2+ clusters in the mouse neonatal neocortex revealed by three-dimensional two-photon Ca2+ imaging in vivo. Neuroimage 138, 64–75. https://doi.org/10.1016/j.neuroimage.2016.05.050.

Lau, C., Ng, L., Thompson, C., Pathak, S., Kuan, L., Jones, A., Hawrylycz, M., 2008. Exploration and visualization of gene expression with neuroanatomy in the adult mouse brain. BMC. Bioinformatics. 9, 153. https://doi.org/10.1186/1471-2105-9-153.

Lei, T., Liao, X., Liang, X., Sun, L., Xia, M., Xia, Y., Zhao, T., Chen, X., Men, W., Wang, Y., Ma, L., Liu, N., Lu, J., Zhao, G., Ding, Y., Deng, Y., Wang, J., Chen, R., Zhang, H., Tan, S., Gao, J.H., Qin, S., Tao, S., Dong, Q., He, Y., 2024. Functional network modules overlap and are linked to interindividual connectome differences during human brain development. PLoS. Biol. 22, e3002653. https://doi.org/10.1371/journal.pbio.3002653.

Leighton, A.H., Lohmann, C., 2016. The wiring of developing sensory circuits—From patterned spontaneous activity to synaptic plasticity mechanisms. Front. Neural Circuits. 10, 71. https://doi.org/10.3389/fncir.2016.00071.

Leopold, D.A., Maier, A., 2012. Ongoing physiological processes in the cerebral cortex. Neuroimage 62, 2190–2200. https://doi.org/10.1016/j.neuroimage.2011.10.059.

Li, Q., Xia, M., Zeng, D., Xu, Y., Sun, L., Liang, X., Xu, Z., Zhao, T., Liao, X., Yuan, H., Liu, Y., Huo, R., Li, S., He, Y., 2024. Development of segregation and integration of functional connectomes during the first 1,000 days. Cell Rep. 43, 114168. https://doi.org/10.1016/j.celrep.2024.114168.

López-Bendito, G., Aníbal-Martínez, M., Martini, F.J., 2022. Cross-modal plasticity in brains deprived of visual input before vision. Annu Rev. Neurosci. 45, 471–489. https://doi.org/10.1146/annurev-neuro-111020-104222.

Luhmann, H.J., 2016. Review of imaging network activities in developing rodent cerebral cortex in vivo. Neurophotonics. 4, 031202. https://doi.org/10.1117/1.nph.4.3.031202.

Luhmann, H.J., Kanold, P.O., Molnár, Z., Vanhatalo, S., 2022. Early brain activity: translations between bedside and laboratory. Prog. Neurobiol. 213, 102268. https://doi.org/10.1016/j.pneurobio.2022.102268.

Luhmann, H.J., Khazipov, R., 2018. Neuronal activity patterns in the developing barrel cortex. Neuroscience 368, 256–267. https://doi.org/10.1016/j.neuroscience.2017.05.025ï.

Luhmann, H.J., Sinning, A., Yang, J.W., Reyes-Puerta, V., Stüttgen, M.C., Kirischuk, S., Kilb, W., 2016. Spontaneous neuronal activity in developing neocortical networks: from single cells to large-scale interactions. Front. Neural Circuits. 10, 40. https://doi.org/10.3389/fncir.2016.00040.

Madisen, L., Garner, A.R., Shimaoka, D., Chuong, A.S., Klapoetke, N.C., Li, L., van der Bourg, A., Niino, Y., Egolf, L., Monetti, C., Gu, H., Mills, M., Cheng, A., Tasic, B., Nguyen, T.N., Sunkin, S.M., Benucci, A., Nagy, A., Miyawaki, A., Helmchen, F., Empson, R.M., Knöpfel, T., Boyden, E.S., Reid, R.C., Carandini, M., Zeng, H., 2015. Transgenic mice for intersectional targeting of neural sensors and effectors with high specificity and performance. Neuron 85, 942–958. https://doi.org/10.1016/j.neuron.2015.02.022.

Martini, F.J., Guillamón-Vivancos, T., Moreno-Juan, V., Valdeolmillos, M., López-Bendito, G., 2021. Spontaneous activity in developing thalamic and cortical sensory networks. Neuron 109, 2519–2534. https://doi.org/10.1016/j.neuron.2021.06.026.

Maruyama, R., Maeda, K., Moroda, H., Kato, I., Inoue, M., Miyakawa, H., Aonishi, T., 2014. Detecting cells using non-negative matrix factorization on calcium imaging data. Neural Netw. 55, 11–19. https://doi.org/10.1016/j.neunet.2014.03.007.

McVea, D.A., Mohajerani, M.H., Murphy, T.H., 2012. Voltage-sensitive dye imaging reveals dynamic spatiotemporal properties of cortical activity after spontaneous muscle twitches in the newborn rat. J. Neurosci. 32, 10982–10994. https://doi.org/10.1523/jneurosci.1322-12.2012.

Meng, X., Mukherjee, D., Kao, J.P.Y., Kanold, P.O., 2021. Early peripheral activity alters nascent subplate circuits in the auditory cortex. Sci. Adv. 7, eabc9155. https://doi.org/10.1126/sciadv.abc9155.

Meunier, D., Lambiotte, R., Bullmore, E.T., 2010. Modular and hierarchically modular organization of brain networks. Front. Neurosci. 4, 200. https://doi.org/10.3389/fnins.2010.00200.

Meunier, D., Lambiotte, R., Fornito, A., Ersche, K.D., Bullmore, E.T., 2009. Hierarchical modularity in human brain functional networks. Front. Neuroinform. 3, 37. https://doi.org/10.3389/neuro.11.037.2009.

Mitchell, A.S., Czajkowski, R., Zhang, N., Jeffery, K., Nelson, A.J.D., 2018. Retrosplenial cortex and its role in spatial cognition. Brain Neurosci. Adv. 2, 2398212818757098. https://doi.org/10.1177/2398212818757098.

Mizuno, H., Ikezoe, K., Nakazawa, S., Sato, T., Kitamura, K., Iwasato, T., 2018. Patchwork-type spontaneous activity in neonatal barrel cortex layer 4 transmitted via thalamocortical projections. Cell Rep. 22, 123–135. https://doi.org/10.1016/j.celrep.2017.12.012.

Mòdol, L., Moissidis, M., Selten, M., Oozeer, F., Marín, O., 2024. Somatostatin interneurons control the timing of developmental desynchronization in cortical networks. Neuron 112, 2015–2030. https://doi.org/10.1016/j.neuron.2024.03.014 e5.

Mohajerani, M.H., Chan, A.W., Mohsenvand, M., Ledue, J., Liu, R., McVea, D.A., Boyd, J. D., Wang, Y.T., Reimers, M., Murphy, T.H., 2013. Spontaneous cortical activity alternates between motifs defined by regional axonal projections. Nat. Neurosci. 16, 1426–1435. https://doi.org/10.1038/nn.3499.

Mojtahedi, N., Kovalchuk, Y., Böttcher, A., Garaschuk, O., 2021. Stable behavioral state-specific large scale activity patterns in the developing cortex of neonates. Cell Calcium 98, 102448. https://doi.org/10.1016/j.ceca.2021.102448.

Moreno-Juan, V., Filipchuk, A., Antón-Bolaños, N., Mezzera, C., Gezelius, H., Andrés, B., Rodríguez-Malmierca, L., Susín, R., Schaad, O., Iwasato, T., Schüle, R., Rutlin, M., Nelson, S., Ducret, S., Valdeolmillos, M., Rijli, F.M., López-Bendito, G., 2017. Prenatal thalamic waves regulate cortical area size prior to sensory processing. Nat. Commun. 8, 14172. https://doi.org/10.1038/ncomms14172.

Nakazawa, S., Iwasato, T., 2021. Spatial organization and transitions of spontaneous neuronal activities in the developing sensory cortex. Dev. Growth Differ. 63, 323–339. https://doi.org/10.1111/dgd.12739.

Nakazawa, S., Yoshimura, Y., Takagi, M., Mizuno, H., Iwasato, T., 2020. Developmental phase transitions in spatial organization of spontaneous activity in postnatal barrel cortex layer 4. J. Neurosci. 40, 7637–7650. https://doi.org/10.1523/jneurosci.1116-20.2020.

Nwabudike, I., Che, A., 2024. Early-life maturation of the somatosensory cortex: sensory experience and beyond. Front. Neural Circuits. 18, 1430783. https://doi.org/10.3389/fncir.2024.1430783.

Oh, S.W., Harris, J.A., Ng, L., Winslow, B., Cain, N., Mihalas, S., Wang, Q., Lau, C., Kuan, L., Henry, A.M., Mortrud, M.T., Ouellette, B., Nguyen, T.N., Sorensen, S.A., Slaughterbeck, C.R., Wakeman, W., Li, Y., Feng, D., Ho, A., Nicholas, E., Hirokawa, K.E., Bohn, P., Joines, K.M., Peng, H., Hawrylycz, M.J., Phillips, J.W., Hohmann, J.G., Wohnoutka, P., Gerfen, C.R., Koch, C., Bernard, A., Dang, C., Jones, A.R., Zeng, H., 2014. A mesoscale connectome of the mouse brain. Nature 508, 207–214. https://doi.org/10.1038/nature13186.

Okujeni, S., Kandler, S., Egert, U., 2017. Mesoscale architecture shapes initiation and richness of spontaneous network activity. J. Neurosci. 37, 3972–3987. https://doi.org/10.1523/jneurosci.2552-16.2017.

O'Leary, D.D.M., Chou, S.J., Sahara, S., 2007. Area patterning of the mammalian cortex. Neuron 56, 252–269. https://doi.org/10.1016/j.neuron.2007.10.010.

Olshausen, B.A., Field, D.J., 2004. Sparse coding of sensory inputs. Curr. Opin. Neurobiol. 14, 481–487. https://doi.org/10.1016/j.conb.2004.07.007.

Omidvarnia, A., Fransson, P., Metsäranta, M., Vanhatalo, S., 2014. Functional bimodality in the brain networks of preterm and term Human newborns. Cereb. Cortex. 24, 2657–2668. https://doi.org/10.1093/cercor/bht120.

Paasonen, J., Stenroos, P., Salo, R.A., Kiviniemi, V., Gröhn, O., 2018. Functional connectivity under six anesthesia protocols and the awake condition in rat brain. Neuroimage 172, 9–20. https://doi.org/10.1016/j.neuroimage.2018.01.014.

Petersen, C.C.H., 2019. Sensorimotor processing in the rodent barrel cortex. Nat. Rev. Neurosci. 20, 533–546. https://doi.org/10.1038/s41583-019-0200-y.

Pnevmatikakis, E.A., Giovannucci, A., 2017. NoRMCorre: an online algorithm for piecewise rigid motion correction of calcium imaging data. J. Neurosci. Methods 291, 83–94. https://doi.org/10.1016/j.jneumeth.2017.07.031.

Powell, N.J., Hein, B., Kong, D., Elpelt, J., Mulholland, H.N., Kaschube, M., Smith, G.B., 2024. Common modular architecture across diverse cortical areas in early development. Proc. Natl. Acad. Sci. u S. a 121, e2313743121. https://doi.org/10.1073/pnas.2313743121.

Quarta, E., Scaglione, A., Lucchesi, J., Sacconi, L., Mascaro, A.L.A., Pavone, F.S., 2022. Distributed and localized dynamics emerge in the mouse neocortex during reach-to-grasp behavior. J. Neurosci. 42, 777–788. https://doi.org/10.1523/jneurosci.0762-20.2021.

Rahn, R.M., Brier, L.M., Bice, A.R., Reisman, M.D., Dougherty, J.D., Culver, J.P., 2022. Functional connectivity of the developing mouse cortex. Cereb. Cortex. 32, 1755–1768. https://doi.org/10.1093/cercor/bhab312.

Ren, C., Komiyama, T., 2021. Characterizing cortex-wide dynamics with wide-field calcium imaging. J. Neurosci. 41, 4160–4168. https://doi.org/10.1523/jneurosci.3003-20.2021.

Rochefort, N.L., Garaschuk, O., Milos, R.I., Narushima, M., Marandi, N., Pichler, B., Kovalchuk, Y., Konnerth, A., 2009. Sparsification of neuronal activity in the visual cortex at eye-opening. Proc. Natl. Acad. Sci. u S. a 106, 15049–15054. https://doi.org/10.1073/pnas.0907660106.

Romano, S.A., Pérez-Schuster, V., Jouary, A., Boulanger-Weill, J., Candeo, A., Pietri, T., Sumbre, G., 2017. An integrated calcium imaging processing toolbox for the analysis of neuronal population dynamics. PLoS. Comput. Biol. 13, e1005526. https://doi.org/10.1371/journal.pcbi.1005526.

Rubinov, M., Sporns, O., 2010. Complex network measures of brain connectivity: uses and interpretations. Neuroimage 52, 1059–1069. https://doi.org/10.1016/j.neuroimage.2009.10.003.

Sestan, N., State, M.W., 2018. Lost in translation: traversing the complex path from genomics to therapeutics in Autism spectrum disorder. Neuron 100, 406–423. https://doi.org/10.1016/j.neuron.2018.10.015.

Shen, J., Colonnese, M.T., 2016. Development of activity in the mouse visual cortex. J. Neurosci. 36, 12259–12275. https://doi.org/10.1523/jneurosci.1903-16.2016.

Shumkova, V., Sitdikova, V., Rechapov, I., Leukhin, A., Minlebaev, M., 2021. Effects of urethane and isoflurane on the sensory evoked response and local blood flow in the early postnatal rat somatosensory cortex. Sci. Rep. 11, 1–13. https://doi.org/10.1038/s41598-021-88461-8.

Siegel, F., Heimel, J.A., Peters, J., Lohmann, C., 2012. Peripheral and central inputs shape network dynamics in the developing visual cortex in vivo. Curr. Biol. 22, 253–258. https://doi.org/10.1016/j.cub.2011.12.026.

Sporns, O., 2013. Network attributes for segregation and integration in the human brain. Curr. Opin. Neurobiol. 23, 162–171. https://doi.org/10.1016/j.conb.2012.11.015.

Stafford, J.M., Jarrett, B.R., Miranda-Dominguez, O., Mills, B.D., Cain, N., Mihalas, S., Lahvis, G.P., Lattal, K.M., Mitchell, S.H., David, S.V., Fryer, J.D., Nigg, J.T., Fair, D. A., 2014. Large-scale topology and the default mode network in the mouse connectome. Proc. Natl. Acad. Sci. u S. a 111, 18745–18750. https://doi.org/10.1073/pnas.1404346111.

Stanley, M.L., Gessell, B., De Brigard, F., 2019. Network modularity as a foundation for Neural reuse. Philos. Sci. 86, 23–46. https://doi.org/10.1086/701037.

Steinmetz, N.A., Buetfering, C., Lecoq, J., Lee, C.R., Peters, A.J., Jacobs, E.A.K., Coen, P., Ollerenshaw, D.R., Valley, M.T., De Vries, S.E.J., Garrett, M., Zhuang, J., Groblewski, P.A., Manavi, S., Miles, J., White, C., Lee, E., Griffin, F., Larkin, J.D., Roll, K., Cross, S., Nguyen, T.V., Larsen, R., Pendergraft, J., Daigle, T., Tasic, B., Thompson, C.L., Waters, J., Olsen, S., Margolis, D.J., Zeng, H., Hausser, M., Carandini, M., Harris, K.D., 2017. Aberrant cortical activity in multiple GCaMP6-expressing transgenic mouse lines. eNeuro 4, 207–224. https://doi.org/10.1523/eneuro.0207-17.2017.

Tabuena, D.R., Huynh, R., Metcalf, J., Richner, T., Stroh, A., Brunton, B.W., Moody, W.J., Easton, C.R., 2022. Large-scale waves of activity in the neonatal mouse brain in vivo occur almost exclusively during sleep cycles. Dev. Neurobiol. 82, 596–612. https://doi.org/10.1002/dneu.22901.

Timme, N.M., Lapish, C., 2018. A tutorial for information theory in neuroscience. eNeuro 5. https://doi.org/10.1523/eneuro.0052-18.2018 eneuro.0052-18.2018.

Townsend, R.G., Gong, P., 2018. Detection and analysis of spatiotemporal patterns in brain activity. PLoS. Comput. Biol. 14, e1006643. https://doi.org/10.1371/journal.pcbi.1006643.

Uhlén, P., 2004. Spectral analysis of calcium oscillations. Science's STKE 2004, pl15. https://doi.org/10.1126/stke.2582004pl15.

Vafaii, H., Mandino, F., Desrosiers-Grégoire, G., O'Connor, D., Markicevic, M., Shen, X., Ge, X., Herman, P., Hyder, F., Papademetris, X., Chakravarty, M., Crair, M.C., Constable, R.T., Lake, E.M.R., Pessoa, L., 2024. Multimodal measures of spontaneous brain activity reveal both common and divergent patterns of cortical functional organization. Nat. Commun. 15, 229. https://doi.org/10.1038/s41467-023-44363-z.

Valley, M.T., Moore, M.G., Zhuang, J., Mesa, N., Castelli, D., Sullivan, D., Reimers, M., Waters, J., 2020. Separation of hemodynamic signals from GCaMP fluorescence measured with wide-field imaging. J. Neurophysiol. 123, 356–366. https://doi.org/10.1152/jn.00304.2019.

Van Den Heuvel, M.P., Kersbergen, K.J., De Reus, M.A., Keunen, K., Kahn, R.S., Groenendaal, F., De Vries, L.S., Benders, M.J.N.L., 2015. The neonatal connectome during preterm brain development. Cereb. Cortex. 25, 3000–3013. https://doi.org/10.1093/cercor/bhu095.

Van Der Bourg, A., Yang, J.W., Reyes-Puerta, V., Laurenczy, B., Wieckhorst, M., Stüttgen, M.C., Luhmann, H.J., Helmchen, F., 2017. Layer-specific refinement of sensory coding in developing mouse barrel cortex. Cereb. Cortex. 27, 4835–4850. https://doi.org/10.1093/cercor/bhw280.

Van Essen, D.C., Glasser, M.F., 2018. Parcellating cerebral cortex: how invasive animal studies inform noninvasive mapmaking in humans. Neuron 99, 640–663. https://doi.org/10.1016/j.neuron.2018.07.002.

Vann, S.D., Aggleton, J.P., Maguire, E.A., 2009. What does the retrosplenial cortex do? Nat. Rev. Neurosci. 10, 792–802. https://doi.org/10.1038/nrn2733.

Warm, D., Bassetti, D., Schroer, J., Luhmann, H.J., Sinning, A., 2022a. Spontaneous activity predicts survival of developing cortical neurons. Front. Cell Dev. Biol. 10, 937761. https://doi.org/10.3389/fcell.2022.937761.

Warm, D., Schroer, J., Sinning, A., 2022b. Gabaergic interneurons in early brain development: conducting and orchestrated by cortical network activity. Front. Mol. Neurosci. 14, 807969. https://doi.org/10.3389/fnmol.2021.807969.

Waters, J., 2020. Sources of widefield fluorescence from the brain. Elife 9, e59841. https://doi.org/10.7554/elife.59841.

White, B.R., Bauer, A.Q., Snyder, A.Z., Schlaggar, B.L., Lee, J.M., Culver, J.P., 2011. Imaging of functional connectivity in the mouse brain. PLoS. One 6, e16322. https://doi.org/10.1371/journal.pone.0016322.

Wu, M.W., Kourdougli, N., Portera-Cailliau, C., 2024. Network state transitions during cortical development. Nat. Rev. Neurosci. 24, 535–552. https://doi.org/10.1038/s41583-024-00824-y.

Yang, J.W., Hanganu-Opatz, I.L., Sun, J.J., Luhmann, H.J., 2009. Three patterns of oscillatory activity differentially synchronize developing neocortical networks In vivo. J. Neurosci. 29, 9011–9025. https://doi.org/10.1523/jneurosci.5646-08.2009.

Yang, J.W., Reyes-Puerta, V., Kilb, W., Luhmann, H.J., 2016. Spindle bursts in neonatal rat cerebral cortex. Neural Plast. 2016, 3467832. https://doi.org/10.1155/2016/3467832.

Yuste, R., Cossart, R., Yaksi, E., 2024. Neuronal ensembles: building blocks of neural circuits. Neuron 112, 875–892. https://doi.org/10.1016/j.neuron.2023.12.008.
Zhang, W., Muravina, V., Azencott, R., Chu, Z.D., Paldino, M.J., 2018. Mutual information better quantifies brain network architecture in children with epilepsy. Comput. Math. Methods Med. 2018, 6142898. https://doi.org/10.1155/2018/6142898.
Zhigalov, A., Arnulfo, G., Nobili, L., Palva, S., Palva, J.M., 2017. Modular co-organization of functional connectivity and scale-free dynamics in the human brain. Netw. Neurosci. 1, 143–165. https://doi.org/10.1162/netn_a_00008.
Zingg, B., Hintiryan, H., Gou, L., Song, M.Y., Bay, M., Bienkowski, M.S., Foster, N.N., Yamashita, S., Bowman, I., Toga, A.W., Dong, H.W., 2014. Neural networks of the mouse neocortex. Cell 156, 1096–1111. https://doi.org/10.1016/j.cell.2014.02.023.